The Canfranc Axion Detection Experiment (CADEx): search for axions at 90 GHz with Kinetic Inductance Detectors

Queries for the author

Please reply to the following queries using the appropriate tool "SEND PROOFS" at the bottom of the preprint page on https://jcap.sissa.it

1. Please check that the names of all authors on the first page are spelt correctly.
2. In JCAP all authors usually appear in the first page with their e-mail address. Please provide only one e-mail address for each author.
3. In JCAP affiliations are written in the form:
   Department, University,
   Street, City, Country
   Please check each affiliation and provide the missing information if needed.
4. Please check that all the images are displayed correctly (order, captions, borders, etc.). Please let us know if there are any problems and provide us with new .pdf, .png, .jpg or .eps file(s) if necessary.
5. If an explicit acknowledgment of funding is required, please ensure that it is indicated in your article. If an Acknowledgments section is already present, please check that the information there is complete and correct.

Journal of Cosmology and Astroparticle Physics
An IOP and SISSA journal

The Canfranc Axion Detection Experiment (CADEx): search for axions at 90 GHz with Kinetic Inductance Detectors

Beatriz Aja,[a] **Sergio Arguedas Cuendis,**[b] **Ivan Arregui,**[c] **Eduardo Artal,**[a] **R. Belén Barreiro,**[d] **Francisco J. Casas,**[d] **Marina C. de Ory,**[e] **Alejandro Díaz-Morcillo,**[f] **Luisa de la Fuente,**[a] **Juan Daniel Gallego,**[g] **Jose María García-Barceló,**[f] **Benito Gimeno,**[h] **Alicia Gomez,**[e] **Daniel Granados,**[i] **Bradley J. Kavanagh,**[d] **Miguel A.G. Laso,**[c] **Txema Lopetegi,**[c] **Antonio José Lozano-Guerrero,**[f] **Maria T. Magaz,**[e] **Jesús Martín-Pintado,**[e,*] **Enrique Martínez-González,**[d] **Jordi Miralda-Escudé,**[b,j] **Juan Monzó-Cabrera,**[f] **Francisco Najarro de la Parra,**[e] **Jose R. Navarro-Madrid,**[f] **Ana B. Nuñez Chico,**[k] **Juan Pablo Pascual,**[a] **Jorge Pelegrin,**[k] **Carlos Peña Garay,**[k] **David Rodriguez,**[e] **Juan M. Socuéllamos,**[d] **Fernando Teberio,**[l] **Jorge Teniente,**[c] **Patricio Vielva,**[d] **Iván Vila,**[d] **Rocío Vilar**[d] **and Enrique Villa**[e]

[a]Departamento de Ingeniería de Comunicaciones, Universidad de Cantabria, Plaza de la Ciencia, 39005 Santander, Spain
[b]Institut de Ciències del Cosmos, Universitat de Barcelona, Martí i Franquès 1, 08028 Barcelona, Spain
[c]Institute of Smart Cities and Dept. of Electrical, Electronic and Communications Engineering, Public University of Navarra, Campus de Arrosadia, 31006 Pamplona, Spain
[d]Instituto de Física de Cantabria (IFCA), CSIC-UC, Avenida de Los Castros s/n, 39005 Santander, Spain
[e]Centro de Astrobiología (CAB), CSIC-INTA, Carretera Torrejón-Ajalvir km4, 28850 Torrejón de Ardoz, Madrid, Spain

[*]Corresponding author.

 https://doi.org/xxxxxxx

[f]Departamento de Tecnologías de la Información y las Comunicaciones,
Universidad Politécnica de Cartagena,
30302 Cartagena, Spain
[g]Centro Astronómico de Yebes, Centro de Desarrollos Tecnológicos (CDT),
Instituto Geográfico Nacional (IGN),
Guadalajara 19080, Spain
[h]Instituto de Física Corpuscular (IFIC), CSIC-University of Valencia,
46980 Valencia, Spain
[i]IMDEA Nanociencia,
Cantoblanco, 28049 Madrid, Spain
[j]Institució Catalana de Recerca i Estudis Avançats,
Barcelona, Spain
[k]Laboratorio Subterráneo de Canfranc,
22880 Canfranc-Estación, Spain
[l]Anteral S.L.,
31006 Pamplona, Spain
E-mail: ajab@unican.es, sarguedas@icc.ub.edu, ivan.arregui@unavarra.es, artale@unican.es, barreiro@ifca.unican.es, casas@ifca.unican.es, mcalero@cab.inta-csic.es, alejandro.diaz@upct.es, fuenterm@unican.es, jd.gallego@oan.es, ???, benito.gimeno@uv.es, agomez@cab.inta-csic.es, daniel.granados@imdea.org, kavanagh@ifca.unican.es, mangel.gomez@unavarra.es, txema.lopetegi@unavarra.es, antonio.lozano@upct.es, mmagaz@cab.inta-csic.es, jmartin@cab.inta-csic.es, martinez@ifca.unican.es, miralda@icc.ub.edu, juan.monzo@upct.es, ???, joser.navarro@edu.upct.es, anunez@lsc-canfranc.es, pascualp@unican.es, jpelegrin@lsc-canfranc.es, cpenya@lsc-canfranc.es, drodriguez@cab.inta-csic.es, socuellamos@ifca.unican.es, fteberio@anteral.com, jorge.teniente@unavarra.es, vielva@ifca.unican.es, vila@ifca.unican.es, ???, evilla@cab.inta-csic.es

Received June 9, 2022
Revised October 18, 2022
Accepted November 4, 2022
Published ???, 2022

Abstract. We propose a novel experiment, the Canfranc Axion Detection Experiment (CADEx), to probe dark matter axions with masses in the range 330–460 μeV, within the W-band (80–110 GHz), an unexplored parameter space in the well-motivated dark matter window of Quantum ChromoDynamics (QCD) axions. The experimental design consists of a microwave resonant cavity haloscope in a high static magnetic field coupled to a highly sensitive detecting system based on Kinetic Inductance Detectors via optimized quasi-optics (horns and mirrors). The experiment is in preparation and will be installed in the dilution refrigerator of the Canfranc Underground Laboratory. Sensitivity forecasts for axion detection with CADEx, together with the potential of the experiment to search for dark photons, are presented.

Keywords: dark matter experiments, axions, dark matter detectors

ArXiv ePrint: 2206.02980

Contents

1 Introduction

Cosmological and astrophysical observations of large-scale structure and the Cosmic Microwave Background Radiation [1–3] indicate the existence of dark matter from its gravitational influence on baryonic matter and radiation. However, it has so far not been otherwise detected. Moreover, independent determinations of the dark matter and baryon cosmic densities based on the measured power spectrum for radiation and matter, the distance-redshift relation, direct mass measurements in galaxy clusters, and the light element abundances from nucleosynthesis, consistently indicate that dark matter constitutes 84.3% of all matter in the universe, with the remaining 15.7% being the known baryonic matter. In spite of this, the nature of dark matter remains a mystery and a key question for particle physics and cosmology.

A particularly attractive dark matter candidate is the Quantum Chromodynamics (QCD) axion: it arises from a theory that solves a fundamental problem in the Standard Model (SM) of particle physics, the strong Charge Conjugation-Parity (CP) problem [4], and at the same time predicts the existence of Cold Dark Matter, which satisfies all present observational constraints. Due to the repeated null results of many worldwide efforts to detect weakly interacting massive particles (WIMPs) [5], which have been the favorite dark matter candidate for the last three decades, the axion dark matter hypothesis has recently attracted increased interest from the experimental community.

The CP problem is the absence of CP violation in the strong force. The expected CP violation arises from the so-called θ-term [6] of the SM Lagrangian for strong interactions.

This term induces an electric dipole moment for the neutron, which has an experimental upper limit of $\sim 10^{-26}\,\mathrm{e}\cdot\mathrm{cm}$ [7], implying $\theta \lesssim 10^{-10}$. There is no reason for this θ-term to be so small compared to unity.

One of the most elegant solution to the CP problem, the Peccei-Quinn (PQ) mechanism [8, 9], introduces a global $\mathrm{U}(1)_{\mathrm{PQ}}$ symmetry and promotes θ to a dynamic field $\theta + a(x)/f_a$, $a(x)$ is the axion field and f_a is the axion scale. At energies below f_a this PQ symmetry is spontaneously broken, generating the pseudo-scalar Goldstone boson known as the axion [10, 11]. The initial value of the background axion field after symmetry breaking is expressed in terms of the misalignment angle $\theta_i = a/f_a$.

Axions can be produced by the vacuum realignment mechanism (by which the axion field returns to the minimum of its potential) [12, 13] with their abundance determined by θ_i. Axions acquire a mass because the $\mathrm{U}(1)_{\mathrm{PQ}}$ symmetry is explicitly broken by the chiral anomaly. The mass of the axion is inversely proportional to the axion scale f_a. Two of the most popular benchmark axion models, the Kim [14], and Shifman, Vainsthein, and Zakharov [15] (KSVZ) model and the Dine, Fischler, Srednicki [16] and Zhitnitsky [17] (DFSZ) model, postulate an f_a significantly above the electroweak scale, consequently producing a very light axion (with mass between µeV and eV).

After the Peccei-Quinn model had been proposed to solve the strong CP problem, the axion was found to be an excellent Cold Dark Matter candidate because of its production mechanism and properties [18–20]. The calculation of the axion relic density (Ω_a) and mass (m_a) depends on the detailed dynamics of the axion field in the presence of complicated finite-temperature QCD effects, resulting in an extensive range of possible masses. Moreover, Ω_a and m_a depend on the cosmic epoch (post or pre-inflation) when the PQ symmetry is broken.

In the pre-inflationary scenario, the PQ symmetry is broken before the end of inflation. In this case, the initial misalignment angle θ_i takes a uniform value throughout space, inherited from a single patch which inflated to become our observable Universe. The axion abundance is then set by this random, unknown value of θ_i. In the post-inflationary scenario, the PQ symmetry is broken after the end of inflation, and the initial misalignment angle θ_i takes on a different value in different causally disconnected regions of the Universe [21]. In this case, it is in principle possible to perform an average over these regions to determine the axion density. Early estimates pointed towards an axion mass range of 4–8 µeV required to account for the entire DM abundance $\Omega_a = \Omega_{\mathrm{DM}}$ [22, 23]. Subsequent work recognised the importance of the production and decay of topological defects such as strings in populating the Universe with DM axions. Simulations accurately resolving these effects remain challenging, but recent estimates point to an axion mass greater than 20 µeV, with viable masses up to $\sim 500\,\mu\mathrm{eV}$ [24–31]. The axion mass range $m_a \gtrsim 40\,\mu\mathrm{eV}$ remains largely unexplored by axion experiments, motivating new experimental searches for heavier DM axions.

The inverse Primakoff effect [32, 33], which converts axions into photons in the presence of a magnetic field, is one method of searching for the axion. The haloscope approach, developed by Sikivie in 1983 [33], searches for axions in the local Galactic dark matter halo using a resonant microwave cavity within high magnetic field. A haloscope transforms some of the halo axions to photons in a spectral line with a central frequency dictated by the axion mass ($\nu_a = m_a c^2/h$) and a line width ($10^{-6} m_a$) determined by the kinetic energy of the axion, proportional to the squared velocity dispersion of the Milky Way dark matter halo in the solar vicinity. Because the mass of the hypothetical axion is unknown, experiments must search a wide frequency range for this spectral line.

Several experiments such as RADES [34], CAPP [35, 36], ADMX [37, 38], ADMX SideCar [39], HAYSTAC [40, 41], QUAX [42, 43], ORGAN [44], GrAHal [45] and others have used this technique to search for axions at frequencies between 400 MHz and 12 GHz (1.65–49.6 µeV). Above 12 GHz, the axion parameter space is heavily unexplored, despite the fact that the post-inflationary scenario suggests that the dark matter axion may well be at higher mass. The main reasons are the difficulty in scaling the haloscope technique to higher frequencies (where the smaller resonant cavities imply a smaller detection volume), and the standard quantum limit to the sensitivity of heterodyne detectors. Beyond this, a number of novel detector concepts, considering broadband haloscopes and single-photon detection systems with potential sensitivities unlimited by the standard quantum limit, have been proposed to cover a wide range of axion masses. These include tunable plasma haloscopes (e.g. ALPHA [46]), dielectric haloscopes [47] (e.g. MADMAX [48]) and dish-antenna haloscopes [49] (e.g. BREAD [50]). Recent reviews of experimental axion searches can be found in [51–53].

The haloscope setup for axion detection is also sensitive to other light, weakly coupled particles, including the dark photon γ'. Dark photons (also known as hidden photons) are vector particles, kinetically mixed with the Standard Model photon [54]. This coupling to electromagnetism induces an electric field in haloscope experiments, providing sensitivity to dark photon dark matter with a mass $m_{\gamma'}$ which matches the resonant frequency of the haloscope (as in the case of the axion) ,without any dependence on the presence of a static magnetic field (unlike the axion). Crucially, such a search can typically be performed using the same data as an axion search or even using calibration data in the absence of a magnetic field [55]. Depending on the polarization state of the dark photon, it may also give rise to a time-varying signal due to the Earth's rotation [56]. Through a careful choice of the observing schedule, it may be possible to detect this time-variation and therefore detect the dark photon. These considerations mean that a dark photon search can typically be performed with little additional experimental exposure time. Dark photons with masses around $m_{\gamma'} \sim 400\,\mu\text{eV}$ correspond to a region of parameter space where bounds on the kinetic mixing are comparatively weak and where sensitivity at the level of $\chi \sim 10^{-9} - 10^{-8}$ would probe new, unconstrained parameter space [56]. In this range, the dark photon can be a viable Dark Matter candidate, produced for example through a realignment mechanism analogous to that of the axion [57–59].

In this work, we propose a novel experiment, the Canfranc Axion Detection Experiment (CADEx), to search for the Dark Matter axion in the mass range (330–460 µeV) within the W-band (80–110 GHz). CADEx combines a microwave resonant cavity haloscope with a broadband incoherent detector system to be installed in the dilution refrigerator in the Canfranc Underground Lab (LSC) [60] in Spain, with the potential for also searching for dark photons.

The paper is organised as follows: in section 2 we compare coherent and incoherent detection techniques. The CADEx concept is described in section 3 and the proposed design of the haloscope, optics and detector components are described in sections 4, 5 and 6, respectively. Finally, sensitivity expectations for the axion-photon coupling and the dark photon kinetic mixing are presented in section 7, and conclusions and future prospects are discussed in section 8.

2 Detection techniques. Coherent versus incoherent

The axion signature is expected as a very narrow emission feature in the frequency domain, and heterodyne receivers are the classical detection systems used in all axion detection experiments at low frequencies (<50 GHz). Heterodyne receivers amplify and convert the input

signal from the haloscope to a lower frequency band, while preserving the information of amplitude and phase. The advantage of this system is that the down-converted signal can be easily processed and digitized to obtain its spectrum (via real-time Fast Fourier Transform) with very high frequency resolution, spectroscopically resolving the radiation generated in the haloscope. The sensitivity floor for the noise temperature of a heterodyne receiver is imposed by the standard quantum noise limit for a coherent detector ($\approx 2.2\,\mathrm{K}$ at $90\,\mathrm{GHz}$ [61]). Very low noise cryogenic W-band heterodyne receivers are routinely used in radio astronomy reaching a state-of-the-art performance noise temperature of $\approx$ 25–30 K[62, 63] when cooled to a physical temperature of 4 K. Practical semiconductor-based heterodyne detectors are not expected to improve from present values (25–30 K) in the short-midterm. The fundamental nature of noise behavior of field-effect transistors (FETs) practically leaves no room for future improvement in noise temperatures of cryogenic amplifiers beyond those already achieved [64]. The effort in the development of cryogenic amplifiers in recent years has been directed towards the expansion of the instantaneous bandwidth which is of importance for the radio astronomy community. Unfortunately this does not help in improving the sensitivity for axion searches with haloscopes since the limiting factor there is the tunability of the cavity.

On the other hand, incoherent detectors, such as those based on bolometers, transition edge sensors (TES), kinetic inductance detectors (KID) or quantum capacitance detectors are not affected by the standard quantum noise limit, as heterodyne receivers are [61]. Their sensitivity is characterized by the Noise Equivalent Power (NEP), defined as the minimum detectable power per square root bandwidth ($\mathrm{W}/\sqrt{\mathrm{Hz}}$) [65], which is limited by photon noise and other factors related to technology. These detectors use superconductor material properties and they can provide high sensitivities in the W-band and in higher frequencies. TES bolometers use a superconductor as a resistive thermometer, whereas the KID detection mechanism exploits the changes of the superconducting kinetic inductance caused by absorbed photons [66]. While TES bolometers operate at the superconducting transition temperature, T_c, KIDs operate at temperatures well below T_c, with conduction electrons in the form of Cooper pairs and identically zero DC resistance. The lowest optical NEP demonstrated so far in a TES bolometer is $3 \times 10^{-19}\,\mathrm{W}/\sqrt{\mathrm{Hz}}$ [67, 68], and KID technology has reached a NEP sensitivity of $3.8 \times 10^{-19}\,\mathrm{W}/\sqrt{\mathrm{Hz}}$ [69].

To make a direct comparison between the sensitivity of the two systems in terms of the NEP, noise temperature and signal-to-noise ratios, we consider idealized coherent and incoherent detectors. Typically, the sensitivity of coherent receivers is described in terms of noise temperature [70], and the signal-to-noise ratio (SNR) is given by

$$\mathrm{SNR}_\mathrm{coh} = \frac{P_\mathrm{s}\sqrt{\tau}}{k_\mathrm{B} T_\mathrm{sys}\sqrt{\Delta\nu}}\,, \tag{2.1}$$

where P_s is the signal power, k_B is the Boltzmann constant, T_sys is the system noise equivalent temperature (sum of the background temperature T_bkg and receiver noise temperature T_rec), with a resolution bandwidth $\Delta\nu$, and integration time τ. In this case, since the spectrum can be resolved, the maximum SNR is obtained by adjusting the resolution of the instrument to the bandwidth of the axion signal ($\Delta\nu = \Delta\nu_\mathrm{s}$). The SNR of an incoherent receiver is

$$\mathrm{SNR}_\mathrm{inc} = \frac{P_\mathrm{s}\sqrt{2\tau}}{\mathrm{NEP}}\,, \tag{2.2}$$

where P_s is the signal power calculated as $k_B T_\mathrm{s} \Delta\nu_\mathrm{s}$ (T_s is the brightness temperature of the signal and $\Delta\nu_\mathrm{s}$ is the signal bandwidth).

The cavity resonant frequency of the haloscope must be tuned to the axion mass, within the haloscope bandwidth $\sim \nu/Q_l$ (where Q_l is the cavity loaded quality factor, defined in section 4), for the axion signal to be produced. The conversion of axions to photons is expected to produce a narrow emission peak of fractional width $\sim 10^{-6}$, determined by the Galactic halo velocity dispersion, in the cavity power spectrum [71]. The cavity generates a peak of linearly polarized thermal noise of bandwidth ν/Q_l, which would ideally be as narrow as the expected signal width but is typically much broader. The noise background, $T_{\rm bkg}$, arises from the blackbody radiation of the surroundings and linearly adds up to the system noise temperature. In our experiment, this contribution arises mainly from the haloscope physical temperature, which can be reduced down to tens of mK, more than one order of magnitude below the intrinsic NEP of the detection system. Therefore, the system noise temperature is dominated by the much higher receiver temperature for a heterodyne receiver, and the background power will also be subdominant for an incoherent detector compared to its typical NEP values.

Considering the case of detection at 90 GHz, the expected axion signal bandwidth is 90 kHz. In this case, a coherent receiver with a state-of-the-art $T_{\rm sys} = 25$ K and an incoherent detector with NEP $= 1.46 \times 10^{-19}\,{\rm W}/\sqrt{\rm Hz}$, (NEP$= k_B T_{\rm sys}\sqrt{2\Delta\nu}$) will provide the same SNR. However, KID technology has the potential to exceed this sensitivity requirement, reaching a NEP around $1 \times 10^{-20}\,{\rm W}/\sqrt{\rm Hz}$ [72]. We therefore consider KIDs as the baseline detector technology for CADEx.

3 Conceptual design

CADEx is going to search for axions in the mass range 330–460 µeV within the W-band (80–110 GHz) by combining the haloscope approach with an incoherent detection system based on KID technology. Incoherent detectors are broad band receivers which do not provide the spectral resolution to detect the narrow-frequency feature produced by the axion in the haloscope. The incoherent detectors in CADEx will measure the linearly polarized axion signal generated in the haloscope against the unpolarized background emission as a function of the resonant frequency of the haloscope. In our design, the switching strategy between the two polarization with a half-wave plate (see below) allows to mitigate the effect of the system gain and background fluctuation in the final sensitivity, by detecting the axion signal in one polarization against the background in the other. The background will be dynamically subtracted from the signal of the axion, mitigating the effect of the system/background gain fluctuation [73].

CADEx will be installed in the dilution refrigerator of the Canfranc Underground Lab (LSC) to decrease the impact of cosmic rays on the final sensitivity using broadband incoherent detectors. Broadband direct detectors are very sensitive to cosmic ray hits. Cosmic rays affect their responsivity by creating glitches on the detected signal which produces net losses of the available useful data, increasing the noise and decreasing the final sensitivity [74]. To achieve the required sensitivity to detect the expected extremely low-level signal of the order of 10^{-24} W, the effect of cosmic rays needs to be minimized in future broadband axion detection experiments. Techniques to mitigate the effect of cosmic rays on KIDs [75] by flagging in the corrupted data can be used for experiments aiming at achieving final sensitivities only few times better than the NEP of the detection system. However, the final sensitivity of the CADEx experiment will be more than 3 orders of magnitude better than the best expected NEPs of $1 \times 10^{-20}\,{\rm W}/\sqrt{\rm Hz}$, making any mitigation technique for cosmic rays contamination very unreliable. The LSC, with a cosmic ray flux of 10^{-4} times that at the surface [76], guaran-

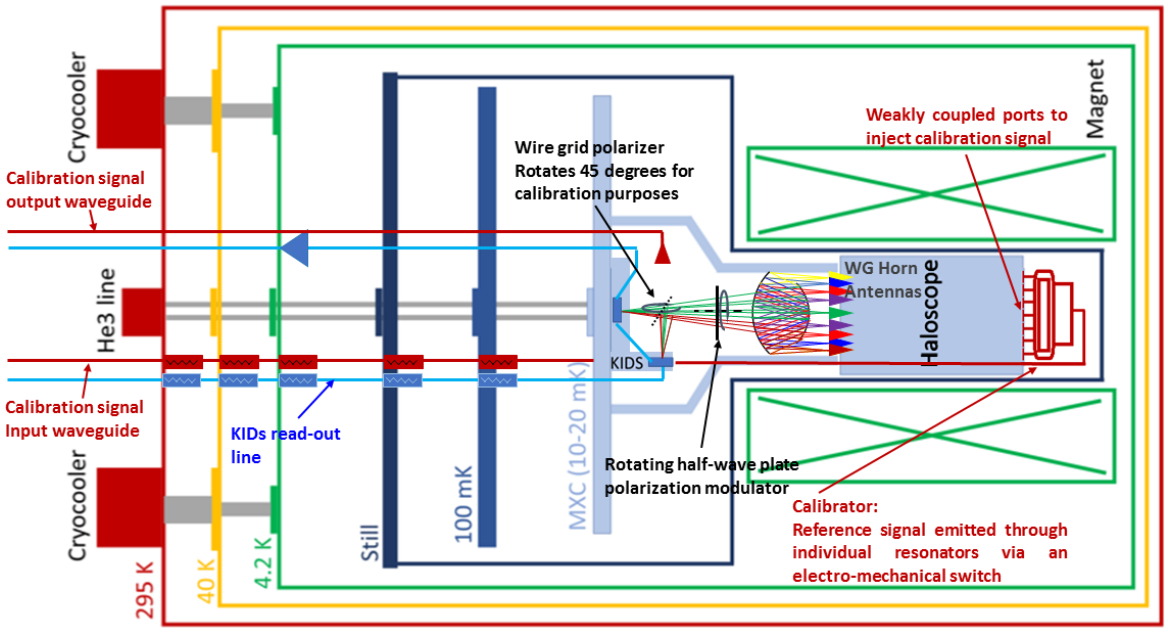

Figure 1. Schematic block diagram proposed for the CADEx's accommodation in the dilution refrigerator of the Canfranc Underground Laboratory. The different temperature stages in the cryostat are indicated with different colors (red: ambient, yellow: 40 K, green: 4.2 K and light blue: 10–20 mK). The 10 T magnet operating at 4 K is depicted by two green boxes with diagonal lines. The main CADEx subsystems installed in the mK stage are also shown: the haloscope (light blue inside the magnet, section 4), the optics (coloured horns and dash dotted rays, section 5) and the two KID arrays to measure two orthogonal linear polarizations (dark blue, section 6). The calibration signal injected externally through the different temperature stages is shown in red (section 5).

tees that CADEX will be able to achieve the required final sensitivities for detector's NEPs of $1 \times 10^{-20}\,\mathrm{W}/\sqrt{\mathrm{Hz}}$with basically no degradation of the sensitivity induced by cosmic rays hits.

Figure 1 shows a block diagram of the experiment accommodated inside the LSC dilution refrigerator, indicating the location of the main subsystems and their temperature. The microwave resonant cavity haloscope described in section 4 will be located in the mK stage to minimize the background radiation seen by the KID detectors, in a static magnetic field of 8–10 T. The radiation from the haloscope will be combined through an optimized quasi-optics system with horns and mirrors (see section 5) and focused on the detection system. As described in section 6, the detection system will make use of radio astronomy techniques [73] to measure the degree of linear polarization of the signal arising from the haloscope, tuned to two adjacent resonant frequencies (see section 4.5). The calibration of the system will be achieved by injecting a polarized signal of known intensity.

4 Haloscope design

Following Sikivie's approach, the haloscope in the detection experiment will be a single cavity or a set of multiple resonant cavities working at the frequency of interest. The detected power

on-resonance from axion-photon conversion is then [77–79]:

$$
\begin{aligned}
P_d &= \frac{\beta}{(1+\beta)^2} g_{a\gamma}^2 \frac{\rho_a}{m_a} B^2 C V Q_0 \\
&= 6.54 \times 10^{-28}\,\mathrm{W} \\
&\quad \times \left(\frac{\frac{\beta}{(1+\beta)^2}}{0.25}\right) \left(\frac{g_{a\gamma}}{1 \times 10^{-15}\,\mathrm{GeV}^{-1}}\right)^2 \left(\frac{\rho_a}{0.4\,\mathrm{GeV\,cm}^{-3}}\right) \\
&\quad \times \left(\frac{370\,\mu\mathrm{eV}}{m_a}\right) \left(\frac{B}{10\,\mathrm{T}}\right)^2 \left(\frac{V}{0.2\,\mathrm{L}}\right) \left(\frac{C}{0.657}\right) \left(\frac{2 \times 10^4}{Q_0}\right),
\end{aligned}
\tag{4.1}
$$

where ρ_a is the dark matter density, and a number of key parameters which depend exclusively on the haloscope design can be identified. These parameters are the cavity volume (V), the form factor (C) of the electromagnetic mode which couples with the axion-photon conversion, the coupling factor for the signal extraction (β), and the unloaded quality factor (Q_0). V, C and Q_0 depend on the cavity geometry and the chosen electromagnetic mode, whereas β depends additionally on the cavity coupling system. Therefore, the operational goals in the design of the haloscope, in order to maximize the detected power and maximizing the sensitivity to $g_{a\gamma}$, is to optimize the coupling β while maximizing V, C and Q_0.

Following the experience in RADES for 8.4 GHz haloscopes [80], we adopt rectangular geometries for the cavities and estimate the above parameters for this type of microwave resonators.

4.1 Form factor

The solenoid magnet in the LSC facility generates a static magnetic field that is constant and parallel to the magnet axis. Therefore, in order to maximize C, an electromagnetic mode with the electric field parallel to this magnetic field must be chosen. In a rectangular cavity, assuming the z-axis as the magnet axis, this is the TM_{110}, with $C = 64/\pi^4 \approx 0.66$ [80].

4.2 Quality factor

The unloaded quality factor for a TM_{110} in a rectangular cavity, assuming only conductor losses, is given by [81]

$$
Q_{0\mathrm{TM}_{110}} = \frac{1}{2}\sqrt{\frac{\pi\sigma}{f_r \varepsilon}} \frac{d\left(a^2+b^2\right)^{\frac{3}{2}}}{ab\left(a^2+b^2\right)+2d\left(a^3+b^3\right)}, \tag{4.2}
$$

where σ is the electrical conductivity of cavity walls, f_r is the mode resonant frequency, ε is the electrical permittivity inside the cavity, which will be normally the vacuum one, ε_0, and a, b and d are the width, height and length of the cavity, respectively. In order to improve this quality factor, full-copper cavities will be employed in CADEx with an expected electrical conductivity around 2×10^9 S/m.

4.3 Volume

The relationship between resonant frequency and rectangular cavity dimensions for both TE_{mnp} and TM_{mnp} modes is given by equation (4.3), where c is the speed of light in free

space, and m, n and p are the number of the sinusoidal variations of the electric field along the x, y and z axes, respectively [81]:

$$f_r = \frac{c}{2}\sqrt{\left(\frac{m}{a}\right)^2 + \left(\frac{n}{b}\right)^2 + \left(\frac{p}{d}\right)^2}\,. \tag{4.3}$$

Taking this into account, detection setups for masses of the order of hundreds of µeV leads to very tiny cavities. As an example, a target resonant frequency of 90 GHz for the TM_{110} mode requires a side of 2.35 mm in a cubic cavity, giving a volume of 13 µL, far from the necessary volume for obtaining acceptable sensitivities. Therefore, since there is plenty of room in the LSC magnet bore, the challenge here is increasing the volume without decreasing the operation frequency of the haloscope. A combination of two different approaches is explored for CADEx.

4.3.1 Large cavities

For the mode TM_{110}, equation (4.3) reduces to

$$f_r = \frac{c}{2}\sqrt{\frac{1}{a^2} + \frac{1}{b^2}}\,, \tag{4.4}$$

which allows us to increase the cavity length (d) without modifying the resonant frequency. Moreover, this resonant frequency is mainly determined by the cavity width (a) when its height (b) is large enough. In that case, increasing the height hardly changes the resonant frequency. Therefore, the volume can be increased with longer and taller cavities. The limit in this enlargement comes from the clustering of modes near the operation mode, which can hinder the detection of the mode through a vector network analyzer (VNA) and even reduce the form factor when two modes are almost overlapped. This problem worsens when a range of frequencies is explored, since the number of mode crossings increases. A trade-off between mode separation and volume can be found by comparing the relative frequency separation between the axion mode and its closest neighbor (with the same polarization) with increasing size of the cavity (height and length), and the loaded quality factor of the axion mode. In this proposal we state initially the height (b) of the cavity in $40a$, which fits with the expected inner dimensions for the magnet bore. Figure 2 shows for this case the relative frequency separation between the axion mode and its closest neighbor (with the same polarization) with increasing lengths, and the relative bandwidth of the resonance for the axion mode ($1/Q_L$). A trade-off between mode separation and volume can be found for $d = 60a$, when the overlapping of mode TM_{111} over TM_{110} begins to be important because this produces a reduction of TM_{110} form factor and difficulties for measuring the quality factor with the VNA. For these cavity dimensions, a separation of 12.5 MHz (0.014%), an unloaded quality factor of 2.2×10^4 and a volume of 11.1 mL are obtained.

4.3.2 Multiple cavities

A larger volume can be obtained by means of the coherent sum of the signal extracted from N resonant cavities, each one resonating at the same frequency. When this occurs, the total detected power is the sum of the powers from each individual cavity. This coherent sum requires the N signals to be in phase at the combining device, in this case the quasi-optical system that will be discussed in the section 5. This is achieved when each signal travels the same electrical length from the cavity-line coupling point to the combining point. An example of

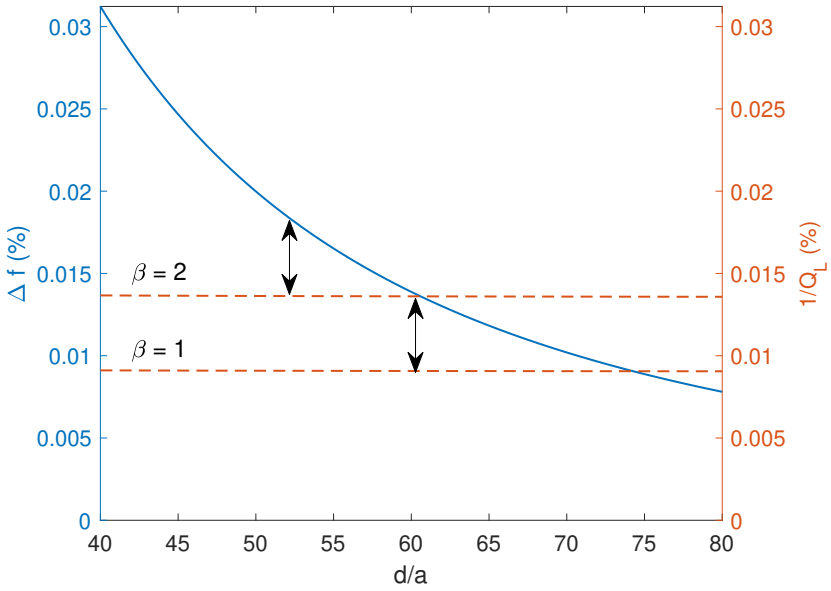

Figure 2. Relative frequency separation (Δf) between modes TM_{110} and TM_{111} and relative bandwidth ($1/Q_L$) of mode TM_{110} in a rectangular cavity when d increases and $b = 40a$.

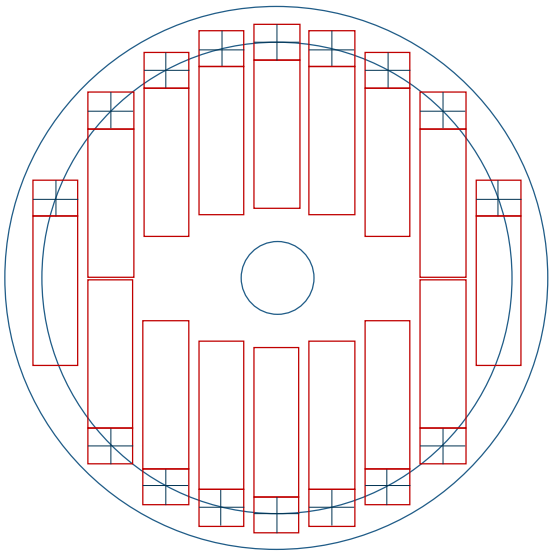

Figure 3. Circumference-arranged multiple cavities (16). Each cavity (red rectangles) is a large cavity (as described in section 4.3.1). The cross at each cavity points out the center of the horn antenna. These antennas are all pointing to a receiver antenna which is located in the center of the circumference, but displaced in the z axis. The scheme is not to scale.

such a configuration, with horn antennas pointing to a centered receiver antenna, is depicted in figure 3 and in figure 10. This setup, assuming a volume of 11.1 mL for each individual haloscope (obtained previously) and coherent sum, produces a total volume of 0.18 L.

4.4 Coupling system

The common coupling system for extracting the energy from a resonant haloscope is a probe connected to a coaxial line. The probe is usually a monopole or a loop, depending on the type of coupling, electric or magnetic, respectively. Nevertheless, this kind of coupling is not useful at W band (75–110 GHz) due to the high attenuation levels of coaxial cables at these high frequencies. Instead, a waveguide connected to a horn antenna is used to transmit the extracted power to the receiver, as explained in the next section. In this case, the coupling element between the cavity and the waveguide is an iris which provides electrical or magnetic coupling [82], depending on the extraction position along the cavity. In this proposal, rectangular irises are used. The coupling of the detection port can be designed to optimize the sensitivity of the experiment at a single central cavity frequency, or the sensitivity over a fixed frequency range to be scanned. For a fixed cavity volume, this optimization is reached in these two cases for $\beta = 1$[1]

Additionally, another port for monitoring the behavior of the cavity, the measurement of the resonant frequency and the quality factor is necessary. Unlike the detection port, this one must be highly decoupled to interfere as little as possible with the detection operation.

Figure 4 shows the half (symmetric) part of a single cavity where the proposed critical coupled and decoupled ports along the cavity are also depicted. In this case, an electrical coupling is used to extract the energy from the cavity towards the detection port. A waveguide bend at the detection port is necessary in order to align the horn connected to this port with the bore axis direction.

Designing accurately an iris for critical coupling at cryogenic conditions is complicated, considering that small contractions in the size of the iris can result in losing the designed coupling. Moreover, the tuning procedure modifies both the resonant frequency of the haloscope and the electric and magnetic field pattern throughout the cavity, which leads losing the critical coupling condition again. Therefore, it is necessary to introduce a moving mechanism which is able to slightly modify the coupling to return to the critical condition. In this proposal, this is implemented by means of a metallic cylinder (screw) which can be introduced or extracted from the waveguide, as shown in figure 5. Figure 6 shows the effect of introducing or extracting this cylinder. From the obtained results, it can be observed that, in this case, the critical coupling is obtained with a penetration depth of 0.1 mm.

4.5 Tuning system

Exploring a wide frequency range in our experiment demands modifying the resonant frequency of each cavity. This can be achieved by modifying the cavity geometry while avoiding a high impact on operational parameters, such as the form factor, quality factor or volume. We propose to modify the cavity width, the geometry parameter that most influences the resonant frequency, by sliding a metallic wall moving along the x axis. This sliding movement

[1]The factor $\kappa = \beta/(1+\beta)$ sometimes appears in the literature and corresponds to the fraction of generated power extracted from the cavity. The critical coupling regime then corresponds to $\kappa = 1/2.$ and $\beta = 2$, respectively (see reference [83]). For our cavity design, the volume of the cavity may be reduced if β is increased, because of the possibility of mode mixing. For example, for the case of figure 2, increasing β from 1 to 2 requires reducing d/a from 60 to 52 (for the same partial ovelaping of resonances between the operation mode and the closest neighbor), implying a volume reduction by the same factor. Taking this into account would yield an optimal value for β to maximize sensitivity over a fixed scanned frequency range that is intermediate between 1 and 2. Moreover, other practical considerations for constructing the cavity with the desired β value while avoiding reflected waves may need to be considered. In this proposal we use $\beta = 1$, although a precise optimized value should be determined for a final design.

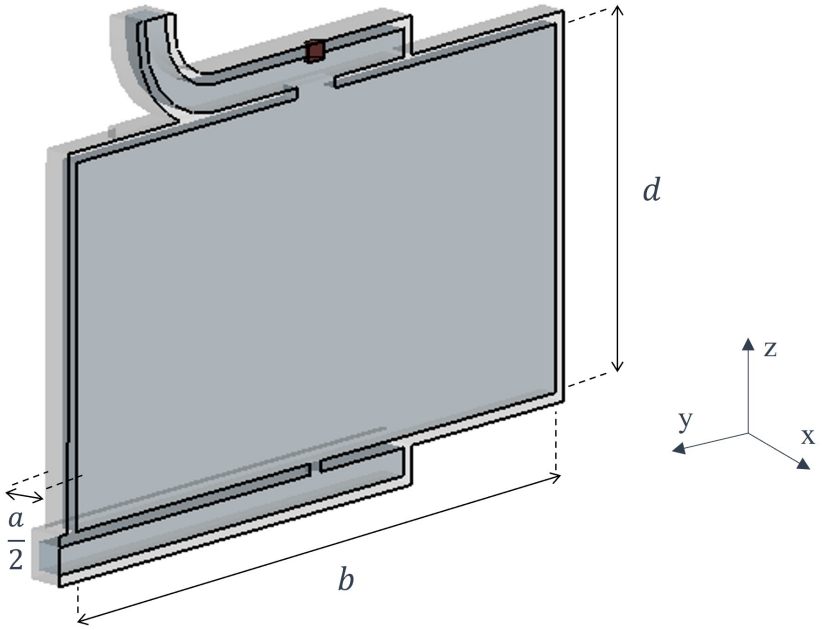

Figure 4. Example of a single cavity with electrical coupling. Half of the structure shown. Upper port corresponds to critically coupled port and lower port corresponds to undercoupled port.

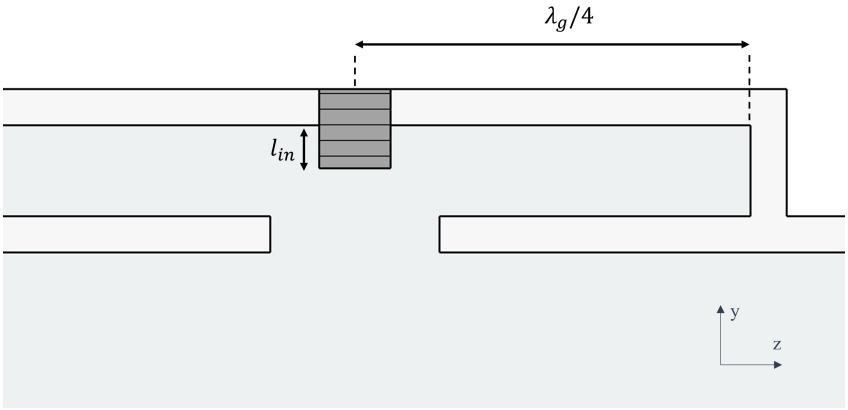

Figure 5. Mechanism of variable coupling system by means of a metallic screw. l_{in} is the screw's length in the waveguide, and λ_g is the wavelength in the waveguide.

is constrained by the coupling iris position and width, and yields a frequency range from 90 to 102 GHz or a 12.5% relative frequency range. This increase in the resonant frequency produces a 5% reduction of the unloaded quality factor, whilst the volume decreases from 11.1 to 9.8 mL.

A common feature in other haloscope experiments during the tuning process is the clustering or even the crossing of modes, which normally leads to strong reduction of key parameters such as the form factor or the quality factor. Graphs of mode crossings and mode

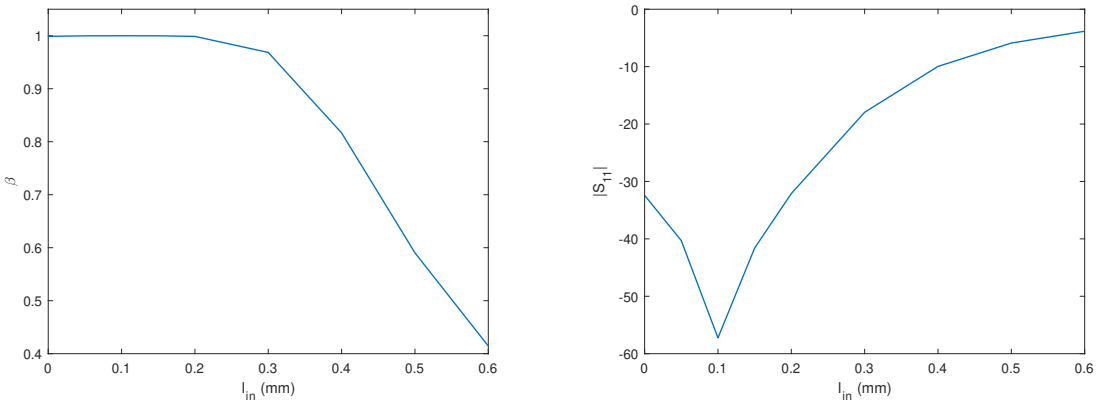

(a) (b)

Figure 6. Coupling factor (β) and magnitude of the reflection coefficient ($|S_{11}|$) in the detection port with the coupling cylinder length.

clustering along the tuning range are presented in figures 7 and 8, respectively. Although figure 7 shows up to 10 mode crossings, all these are of high-order TE modes. The electric field for TE modes is normal to the static magnetic field from the solenoid and, therefore, they are not coupled with the photons generated by the Primakoff effect (in other words, the form factor is zero). Moreover, these modes are not coupled to the waveguide through the iris and, therefore, their resonances (due to the noise) are not detected and do not overlap with the TM_{110} resonances. Nevertheless, degenerate TE and TM modes can slightly couple due to imperfections in manufacturing, and the mode crossings can still affect the haloscope performance at those frequencies. On the other hand, as seen in figure 8, the mode clustering due to the large size of the cavity can even worsen when the width of the cavity is reduced in order to scan higher masses. But, as shown, the worsening of the clustering of modes TM_{110} and TM_{111} is relatively small.

The tuning mechanism by means of a sliding wall is a technological challenge. In order to keep a high cavity quality factor, it is very important to get good electrical contact between the sliding part and the inner walls of the cavity. Figure 9 shows the concept of the sliding wall, where a double mechanism for providing a short-circuit in the contacts between the sliding wall and the surrounding walls is depicted. First, a choke is included behind the moving wall by means of a stub. The short-circuit provided by this stub is, by nature, resonant and, therefore, it is not expected a good behavior for the whole scanning range. Nevertheless, high-performance broadband sliding short-circuits [84] could be used. The manufacturing of this device, taking into account the small width of the cavity is a major challenge in this design. Second, a gasket part surrounding the wall provides metallic contact between the sliding wall and the inner walls of the cavity. Although the combination of both systems will provide a good short-circuit condition, it is expected to result in a small reduction of the quality factor, in the order of 10%.

5 Optics design and calibration system

To optimize the sensitivity of the experiment, the extremely weak axion signal (as previously mentioned, of the order of 1×10^{-24} W generated at the haloscope cavities must be guided

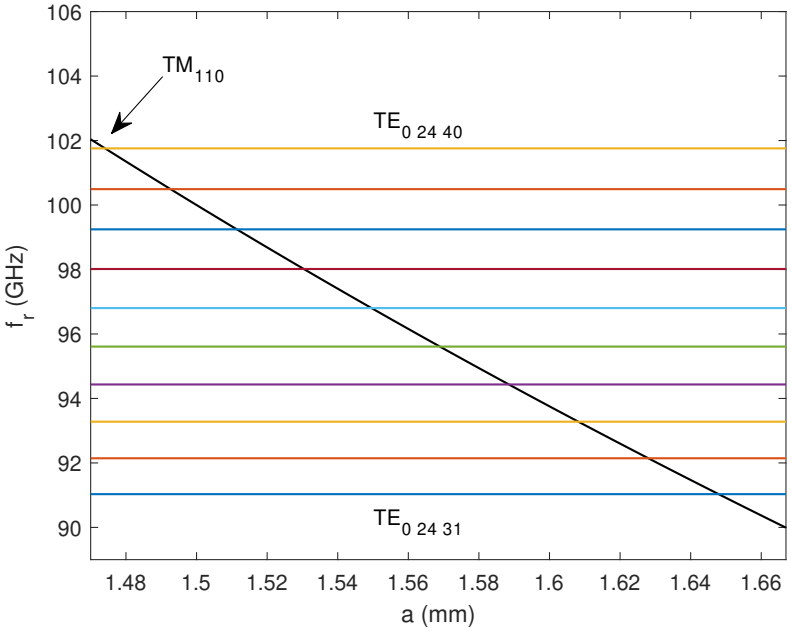

Figure 7. Mode crossing along the scanning range among TM_{110} and $TE_{0,24,p}$ modes with p ranging from to 31 to 40 for a cavity with $a = 1.66$ mm, $b = 40a$, $d = 60a$.

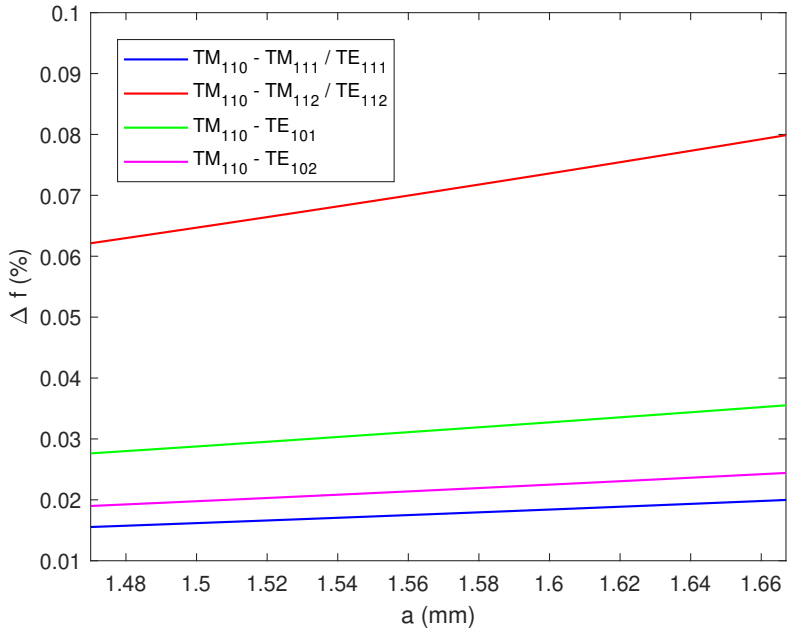

Figure 8. Relative closeness of neighbor modes to the TM_{110} along the scanning range for a cavity with a = 1.66 mm, $b = 40a$, $d = 60a$.

in phase with minimal losses to the detection system. For W-band, quasi-optical guiding of the signal by means of reflection at several mirrors is the most efficient method.

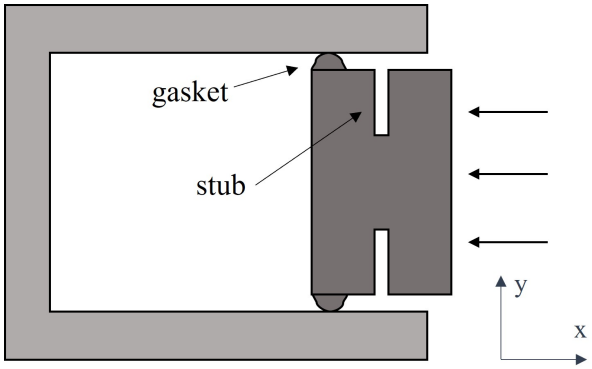

Figure 9. Tuning mechanism with sliding wall.

The overall optical system design is schematically presented in figure 1 and a more detailed view is shown figure 10. The optics is designed to collect, redirect and collimate the signals from each individual cavity of the haloscope onto the KID detector array. The optics and the haloscope are designed to guarantee the phase coherence among the cavities at the detectors, using the haloscope configuration shown in figure 3, where all cavities are arranged in a circumference to have the same optical path from the haloscope to the detectors, so indeed all the signals will be added coherently at the detector region and special care must be taken to reduce misalignment errors that can change the phase and drive a reduction in received power. To reduce misalignment errors, these reflectors will not move during operation and/or calibration and in fact the individual sixteen outer mirrors will be manufactured in a single piece. In addition, the optics design minimizes phase aberration by reducing path length differences in all mirrors, which are also large enough, (at least three beamwaist), to minimize spillover losses. However, the final detailed design optimizing spillover losses, horn antennas, path length, etc. will be finalized according to the final cryostat mK stage dimensions.

The proposed design (see figure 10) is based on a double reflector configuration that fits into the available cryostat volume. Each haloscope WR-10 standard waveguide output is fitted with a horn antenna that radiates over an outer smaller elliptical mirror whose foci are located in the horn antenna phase centre and in the line that connects the middle of the haloscope array and the detector. The optical system is composed of sixteen identical horns and mirrors that share the second focus position. All the radiation is collected with a bigger symmetrical elliptical reflector whose foci are located in the line that connects the middle of the haloscope array and the detector area, the nearest focus is located in the same position as the one shared by the sixteen outer smaller elliptical mirrors around. The shape of the bigger reflector is designed to focus the cavity beams in the detector focal plane with identical path length for every haloscope cavity. Before reaching the KID detectors, see figure 1, the signal is modulated with a rotating half wave plate (black vertical line) and split in the two polarizations by a wire grid polarizer (tilted dotted line), allowing the full characterization of the signal's linear polarization.

The design considers a calibration system based on the application of a Synthetic Axion Generator, similar to the one used in the ADMX experiment [85]. In our case, a millimeter-wave signal mimicking the one generated by the axion in a resonant cavity will be synthesized by a pulse signal generator and a high frequency analog signal generator. The signal will be injected into the resonant cavities by their weakly coupled ports. Such calibration will be achieved individually for each resonant cavity via the use of an electro-mechanical WR-10

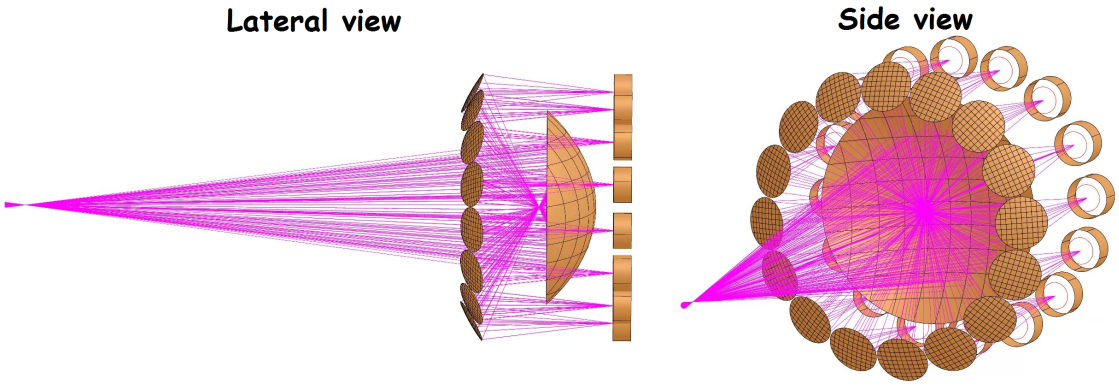

Figure 10. Quasi Optical system design. In this figure ray optics simulation is shown where sixteen horn antenna apertures are allocated in a circumference to match the haloscope multiple resonant cavities configuration seen in figure 3. Each individual horn radiation is redirected towards a main central elliptical mirror that focuses all the radiation symmetrically in the detector area.

standard waveguide switch with one input and sixteen outputs, see figure 1. Calibration signal response will be received via a horn antenna allocated in the opposite direction of one of the KID detectors areas. The beam with calibration power will be redirected to such horn antenna through a 90 degrees rotation of the wire grid polarizer, see figure 1. The calibration system will also be used to test the functionality of the experiment.

6 Detection system: kinetic inductance detectors

The CADEx detection system will be based on state-of-the-art superconducting Kinetic Inductance Detectors (KIDs), which are high quality factor superconducting resonators indirectly coupled to a single transmission line. The working principle is based on the variation of superconducting properties caused by incoming radiation. Absorbed photons change the quasiparticle density which modifies the kinetic inductance of the resonator, lowering the resonant frequency and diminishing the quality factor of the resonator. As usual for pair-breaking detectors, the cut-off frequency that can be absorbed is limited by twice the superconducting gap, $2\Delta \approx 3.52\, k_{\rm B} T_{\rm c}$, where $k_{\rm B}$ is the Boltzmann constant and $T_{\rm c}$ the superconducting critical temperature [86]. Therefore, the detection in W-band intended in the CADEx experiment requires employing a Titanium (Ti)/Aluminium (Al) bi-layer approach, which has demonstrated good sensitivity down to 80 GHz [87]. Optimal performance of KIDs is achieved when detectors are cooled down well below their critical temperature ($T_{\rm op} < T_{\rm c}/6$), so a cryogenic system with base temperature $\sim$ 100 mK is planned. Moreover, these superconductor detectors are individually adjusted for each KID by means of its resonant frequency, making them inherently multiplexable in the frequency domain, allowing thousands of pixels to be read-out over a single transmission line [88, 89].

KID arrays will be implemented to guarantee that the final expected sensitivity from CADEX will be achieved. The largest signal to noise ratio will be obtained by focusing all the energy from the haloscope on a single KID detector. However, the beam from the haloscope is gaussian and even for the best match coupling of the haloscope beam to a square KID pixel the system will waste some signal from the haloscope. Having pixels surrounding the central detector will have the benefit of detecting all the energy arising from the haloscope. Additional pixels outside the haloscope beam area will be used to measure the non-polarized

background emission with high precision by averaging as many pixels as possible. Then, the final sensitivity of the detected signal after dynamically subtracting the background will be not affected by the noise of the background, keeping the signal noise close to the NEP and not to $\sqrt{2}\times$NEP. A number of pixels in the array will be blind dark pixels allowing to correct for the systematic noise introduced by the read out electronics.

KIDs have been developed in the context of astronomical experiments, demonstrating state-of-the-art sensitivity ranging from the millimeter to the ultraviolet range [73, 90]. Also, future far-infrared (FIR) missions such as the Origins Space Telescope have selected KIDs as their base technology [72]. KIDs have also been proposed for dark matter experiments as indirect detectors via the absorption of athermal phonons [91, 92] or, more recently, as direct photon detectors through a broad-band haloscope [50].

The baseline of the detection system for CADEx aims at lumped-element KIDs (LEKIDs), where the superconducting inductor acts as the effective optical absorber of the incident radiation. To maximize the optical efficiency, the inductor geometry should be matched to the free-space impedance optimizing the meander geometry, substrate and superconducting material thicknesses and back-short distance [93].

The resonant frequency shift of the LEKIDs is read out by a single transmission line coupled to the detectors. This coupling coefficient can be tuned using low-frequency simulations by changing the separation to the line. The LEKIDs response is maximized when critical coupling is achieved under the desired optical load, or when the external quality factor (Q_c) equals the internal quality factor (Q_i). Since Q_i is set by fixed parameters such as the optical background or operating base temperature, Q_c will be optimized by tuning the geometrical parameters [93].

The CADEx experiment will search for the axion using the expected signal polarization generated in the haloscope. To measure the polarization, the detection system will follow the configuration of the polarimeters used in radio astronomy operating at frequencies above 90 GHz like NIKA2 at the IRAM 30 m telescope [73, 94]. Basically, the radiation from the haloscope will be first modulated by a half-wave polarization modulator followed by a grid polarizer which separates the two orthogonal linear polarizations to be simultaneously detected by two different LEKIDs arrays perpendicularly oriented and sharing the same read-out line. The LEKIDs will be based on a fractal Hilbert geometry with no preferential polarization direction in absorption [94], avoiding the critical alignment between the linear polarization direction of the incident electromagnetic field from the haloscope and the detector at low temperatures. Figure 11 shows a preliminary single LEKID design with a Hilbert geometry and its simulated absorption for two orthogonal polarizations at W-band, as well as a visualization of an array assembled on a holder for its characterization. The proposed design allows for characterization of the polarization from the axion-photon conversion and simultaneous subtraction of the unpolarized background, for all the observing time.

A key parameter for this experiment is the ultimate sensitivity of the detection system, the NEP, defining the weakest signal detectable by the detector. Special attention is paid to the maximum allowable magnetic field in the KIDs focal plane, which can degrade their sensitivity, lowering their quality factor and increasing system noise and NEP. Thus, a dedicated magnetic shield and vortex traps will be developed for minimizing the effects of the magnetic field on the final sensitivity, keeping the magnetic field below 10 µT [95]. The sensitivity of KIDs at low radiation power is limited by the generation and recombination of quasi-particles in thermal equilibrium, which depend on superconducting properties. Visser et al. have already reached this limit, NEP $= 3.8 \times 10^{-19}\,\mathrm{W}/\sqrt{\mathrm{Hz}}$, in a low background configuration [69].

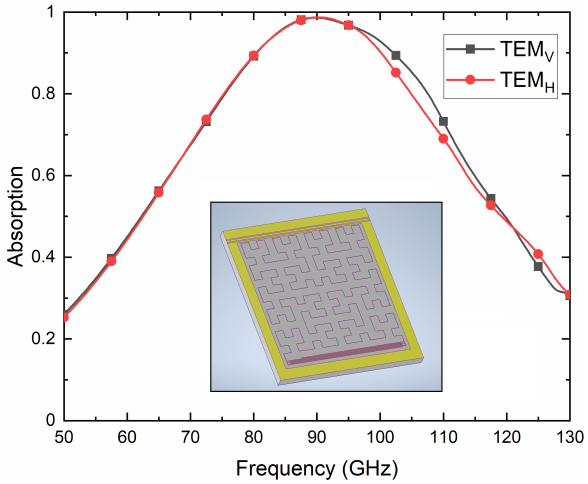

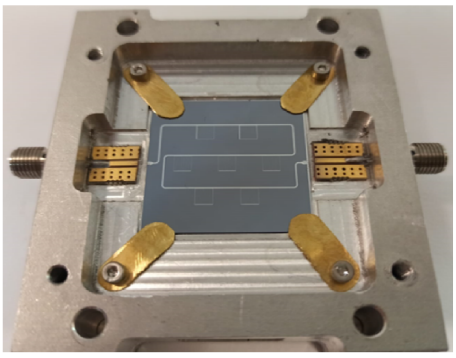

Figure 11. Left: single LEKID using a Hilbert geometry (3 mm x 3 mm cell) and absorption efficiency simulated at the W-band; Right: seven KIDs array mounted on an aluminum holder.

Nevertheless, several strategies such as volume reduction and optimization of the two-level system (TLS) noise predict the potential for further improvement in sensitivity down to $1 \times 10^{-20}\,\mathrm{W}/\sqrt{\mathrm{Hz}}$, reaching the ultimate sensitivity for the proposed experiment [72].

7 Projected axion sensitivity

In order to estimate the sensitivity of CADEx to axion-photon conversion and other signals, we compare the detected signal power P_d with the expected noise in the measured power in the detector σ_P. For the design parameters of the CADEx experiment summarized in table 1, the SNR is given by equation (2.2). The signal power for axion-photon conversion is given in equation (4.1). The reach of a haloscope experiment in terms of the axion-photon coupling $g_{a\gamma}$ at a desired SNR is therefore given by [96, 97]:

$$\begin{aligned} g_{a\gamma}[\mathrm{GeV}^{-1}] &= \left(\frac{3.88\times10^{2}}{B[\mathrm{T}]}\right)\sqrt{\frac{(1+\beta)^2}{\beta}}\sqrt{\frac{\mathrm{SNR}\,m_a[\mathrm{eV}]\,\mathrm{NEP}[\mathrm{W}/\sqrt{\mathrm{Hz}}]}{V[\mathrm{L}]\,Q_0\,t[\mathrm{s}]^{\frac{1}{2}}\,C}} \\ &= 3.88\times10^{-13}\mathrm{GeV}^{-1} \\ &\quad\times\left(\frac{10\mathrm{T}}{B}\right)\left(\frac{0.25}{\frac{\beta}{(1+\beta)^2}}\right)^{\frac{1}{2}}\left(\frac{\mathrm{SNR}}{5}\right)^{\frac{1}{2}}\left(\frac{m_a}{3.7\times10^{-4}\,\mathrm{eV}}\right)^{\frac{1}{2}} \\ &\quad\times\left(\frac{\mathrm{NEP}}{1\times10^{-19}\,\mathrm{W}/\sqrt{\mathrm{Hz}}}\right)^{\frac{1}{2}}\left(\frac{0.2\mathrm{L}}{V}\right)^{\frac{1}{2}}\left(\frac{2\times10^{4}}{Q_0}\right)^{\frac{1}{2}}\left(\frac{3\text{ months}}{t}\right)^{\frac{1}{4}} \\ &\quad\times\left(\frac{0.66}{C}\right)^{\frac{1}{2}}. \end{aligned} \tag{7.1}$$

The projected 5σ sensitivity of CADEx is shown in figure 12. The vertical black dashed line corresponds to a three months search centered on an axion mass of $m_a \sim 370\,\mu\mathrm{eV}$. This search would achieve a sensitivity down to $g_{a\gamma} \approx 4\times10^{-13}\,\mathrm{GeV}^{-1}$.

Exploring a wider range of axion masses requires a large number of searches with the haloscope tuned to different resonant frequencies ν_c. The cavity bandwidth is $\Delta\nu_c = \nu_c/Q_\ell \approx$

Parameter	Symbol	Value
Axion DM Density	ρ_a	$0.45\,\mathrm{GeV\,cm^{-3}}$
Total cavity volume	V	0.2 L
Magnetic field	B	8–10 T
Unloaded quality factor	Q_0	2×10^4
Coupling factor	β	1
Form factor	C	0.66
Axion mass	m_a	330–460 μeV
Noise equivalent power	NEP	1×10^{-19} (3×10^{-20}) $\mathrm{W}/\sqrt{\mathrm{Hz}}$

Table 1. Design parameters for the CADEx experiment.

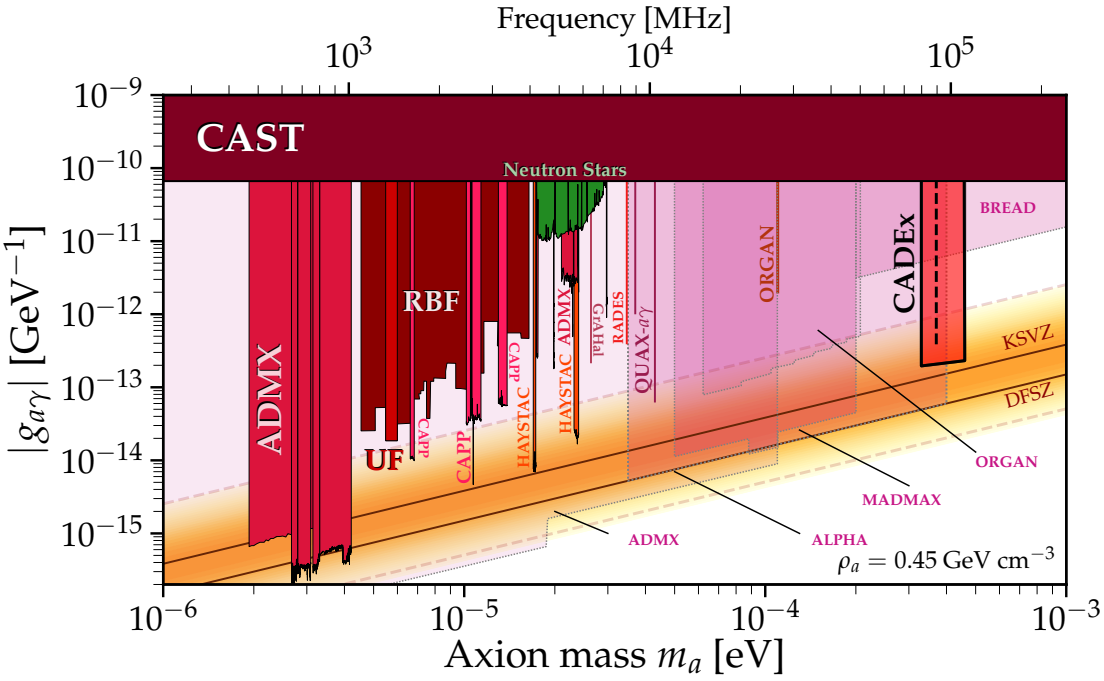

Figure 12. *Projected CADEx sensitivity to the axion-photon coupling* $g_{a\gamma}$. The vertical black dashed line corresponds to the 5σ sensitivity (SNR = 5) of 3 months exposure with noise equivalent power NEP $= 1 \times 10^{-19}\,\mathrm{W}/\sqrt{\mathrm{Hz}}$. The region bounded by a solid black line corresponds to the sensitivity with roughly 3000 1-day exposures, $Q_0 = 2 \times 10^5$ and $3 \times 10^{-20}\,\mathrm{W}/\sqrt{\mathrm{Hz}}$, achievable on a timescale of $\mathcal{O}(8)$ years. For comparison, we show a number of existing constraints from the CAST helioscope [98], various axion haloscopes (filled red and purple regions) [34, 36–38, 40, 41, 43–45, 99–104], and neutron stars [105], along with projected constraints from other proposed haloscopes (transparent red regions) [44, 46, 48]. Figure adapted from [106].

9 MHz. A frequency range of 30 GHz (corresponding to axion masses 330–460 μeV) could be covered with ~ 3000 exposures. Assuming that a NEP of $3 \times 10^{-20}\,\mathrm{W}/\sqrt{\mathrm{Hz}}$ can be achieved with future technology and one could in principle gain an order of magnitude on the Q_0 using superconducting cavities [107], sensitivity down to $g_{a\gamma} \approx 2 \times 10^{-13}\,\mathrm{GeV}^{-1}$ can be achieved

in a single exposure of $\sim$ 1 day. The mass range 330–460 µeV could therefore be probed on a total measuring time of $\sim$ 8 years (which can be split among several instruments with haloscopes build for different frequency ranges), shown by the region bounded by a thick black solid line in figure 12.

For comparison, we also show in figure 12 a number of existing constraints from axion haloscopes, from neutron stars observations and from the CAST helioscope. These provide constraints on the axion parameter space for $g_{a\gamma} \gtrsim 7 \times 10^{-11}\,\mathrm{GeV}^{-1}$ and for $m_a \lesssim 50\,\mu\mathrm{eV}$. CADEx would probe unexplored parameter space at higher masses, well-motivated by cosmological production mechanisms, reaching into the region of axion-photon couplings suggested by QCD axion theory [108–110], shown by the yellow band in figure 12. CADEx would be complementary to other proposals using established search techniques with resonant cavities, such as ADMX [111] and ORGAN [44], which should have sensitivities up to masses of 200 µeV, as well as alternative broadband detector concepts such as ALPHA, MADMAX and BREAD.[2]

An important advantage of our KIDs detection system is that modulating the haloscope signal as a function of polarization allows for distinguishing the axion signal from background unpolarized systematics. A true axion signal is detected as an excess of power in one of the frequency channels scanned by the haloscope over the neighboring ones, which appears only in the polarization expected for the axion. The proportionality of the signal to B^2 can also be tested.

7.1 Dark photon sensitivity

Constraints on dark photons can be derived similarly to constraints on axions and axion-like particles. The signal power due to the resonant conversion of dark photons can be obtained from equation (4.1), using the correspondence [55, 58]:

$$g_{a\gamma} \to \frac{\chi m_{\gamma'} \sqrt{\cos^2\theta_{\mathrm{pol}}}}{B}\,, \tag{7.2}$$

where we assume that the dark photons account for all of the local DM. Here, χ is the kinetic mixing parameter and θ_{pol} is the angle between the polarization vector of the dark photon field and the electric field polarization to which the detector is sensitive. Using the detection system described in section 6, we propose to measure the two orthogonal linear polarizations of the radiation from the cavity. However, the cavity is oriented such that the electric field direction of the TM_{110} mode lies parallel to the external B-field (see section 4). Therefore only the component of the dark photon polarization parallel to this direction can contribute to the resonant conversion signal. In this case, then, θ_{pol} is the angle between the dark photon polarization and the external B-field.

Depending on the cosmological production and evolution of the dark photon field (e.g. [112–115]), the dark photon may be polarized along a fixed direction on long timescales compared to the integration time of the experiment at a given frequency channel. In this case, the dark photon polarization remains fixed but θ_{pol} varies with time as the orientation of the detector changes with the Earth's rotation. This gives rise to a periodic signal $P(t) \propto \cos^2\theta_{\mathrm{pol}}(t)$ with a period of 1 day and an $\mathcal{O}(1)$ oscillation amplitude [56]. In this scenario, the detection of a time-varying polarized signal could be used to discriminate from

[2]We plot projections for BREAD assuming 1000 days of exposure and baseline assumptions on NEP from reference [50].

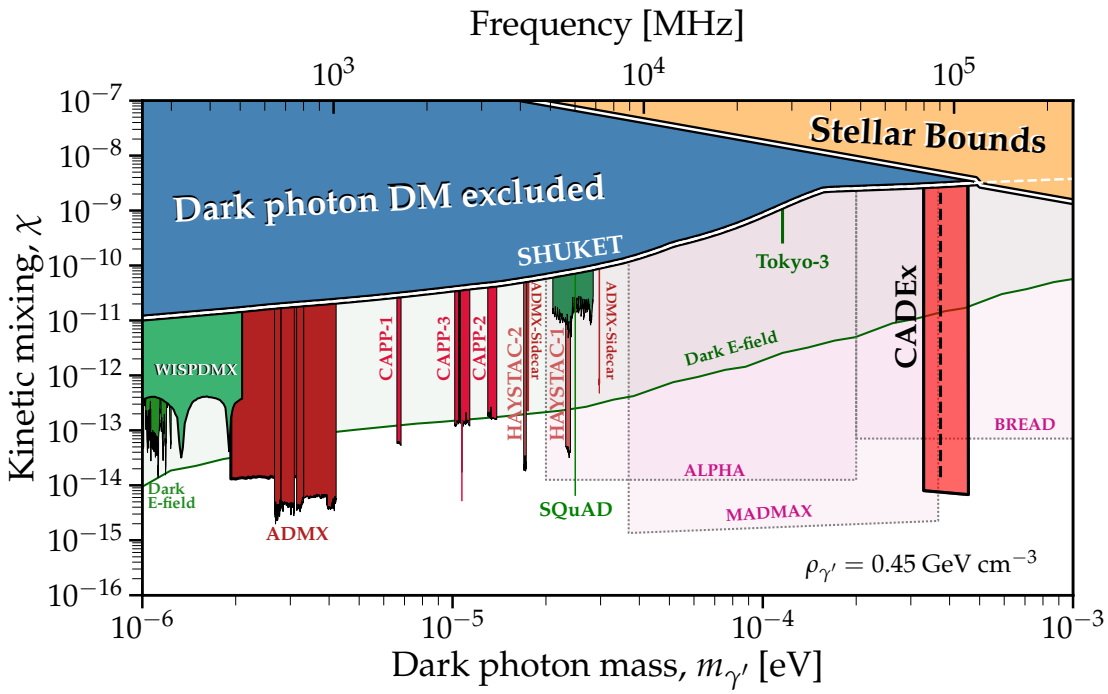

Figure 13. *Projected CADEx sensitivity to the dark photon kinetic mixing χ.* The region labelled "CADEx" is the sensitivity achievable using the same searches as presented in figure 12 (with no additional data taking). The solid blue regions show where dark photons are excluded from being all of the Dark Matter on cosmological grounds [56, 58]. The orange region shows the envelope of constraints from stellar cooling (see [56] for a compilation). We show current and projected constraints from other axion haloscopes in red, with dedicated dark photon searches shown in green [116–120]. Figure adapted from [56] and [106].

backgrounds and claim a discovery of the dark photon, as long as the dark photon polarization remains constant on timescales longer than ~ 1 days (the duration of each mass scan).

The value of $\theta_{\rm pol}$ averaged over long timescales depends on the detector orientation and the dark photon polarization direction. We therefore fix $\langle \cos^2 \theta_{\rm pol} \rangle = 1/3$, the average over randomly oriented dark photon polarization angles [56]. This factor of 1/3 can be intuitively understood from the fact that at any given time, the detector will be sensitive to only one of the three possible polarization directions of the dark photon (the one parallel to the electric field direction of the TM_{110} mode of the cavities). Under these assumptions, it is possible to map the projected sensitivities in the axion parameter space $(m_a, g_{a\gamma})$ to the dark photon reach in $(m_{\gamma'}, \chi)$, using equation (7.2).

In figure 13, we show the 5σ sensitivity to the dark photon kinetic mixing which can be achieved by CADEx in this constant, fully polarized dark photon scenario, using the same data taken for the axion search described above and presented in figure 12. CADEx should be sensitive to values of $\chi \sim 10^{-14}$ for dark photon masses in the range 330–460 µeV. Existing constraints in this region are at the level of $\chi \sim 10^{-9}$, where cosmological constraints [56, 58] and stellar cooling constraints [56] intersect. CADEx will therefore significantly enhance sensitivity in this region of dark photon parameter space.

We have so far considered the fixed, full polarization scenario for the dark photon. However, the evolution of the dark photon through structure formation may wash out any

initial large-scale polarization which may be present. In an unpolarized scenario, the resulting photon signal would also be unpolarized, with no time-variation to distinguish it from backgrounds. Moreover, the dark photon signal does not rely on the presence of the magnetic field, meaning that it is not easy to obtain a 'background-only' data set for comparison. In principle, it may still be possible to set limits on χ, by searching for a change in the intensity measured by the KID detector at a frequency channel compared to neighboring ones. However, this would require a good control of systematics in the absolute power calibration of the KIDs detectors and in any background radiation in the experiment over a range of frequencies. In the unpolarized scenario, then, figure 13 would represent the most optimistic possibility for setting limits on χ. However, we emphasize that the ability to set a limit in this scenario depends on whether absolute background systematics can be corrected, which is unclear at this stage. In any case, a more detailed understanding of the expected polarization of the dark photon in the Milky Way will be essential to characterize this signal in the future.

8 Conclusions

The QCD axion arises naturally as an extension of the Standard Model to solve the strong CP problem. Simultaneously, axions may be produced with the correct abundance in the early Universe to provide the current cold dark matter content. Haloscopes are being widely used to search for the QCD axion in the mass range 1.65–49.6 µeV. However, searches for the axion above this mass range, well motivated by theory, have not yet been performed primarily due to a number of technological challenges in haloscopes and in the detection system. Overcoming these challenges will allow sensitive searches for axions in the dark matter halo with masses in the range 100–1000 µeV, as well as other light new particles such as the dark photon.

This paper presents CADEx, a novel experiment to search for the Dark Matter QCD axion and dark photon in the unexplored mass range 330–460 µeV operating within the W-band at the Canfranc Underground Laboratory (Spain). CADEx will push the microwave resonant cavity haloscope technology to high frequencies, increasing its collecting power by means of the coherent sum of multiple large cavities. The detection system uses the polarization properties of the axion signal arising from the haloscope, and is based on broadband Kinetic Inductor Detectors (KIDs) with sensitivities that have a strong improvement potential in the near future. When equipped with a 0.2 L haloscope in a high and static magnetic field of 8–10 T and a detection system with KIDs sensitivities of $3 \times 10^{-20}\,\mathrm{W}/\sqrt{\mathrm{Hz}}$, CADEx will provide a sensitivity three orders of magnitude better than the current best limit from CAST [34], reaching the well-motivated region for QCD axion dark matter predicted from models [108–110].

The same setup will also provide sensitivity down to a dark photon kinetic mixing of $\chi \sim 10^{-14}$ over the same range of masses, for the case where the dark photon is fully polarized. This would provide around 5 orders of magnitude improvement over current constraints, in a region of parameter space where the dark photon may account for all of the dark matter [58] while constraints from stellar cooling are weak [56]. Although it is not clear at present if these constraints can still be obtained when the dark photon is unpolarized, we note that the dark photon search can be performed with data obtained when the magnetic field is turned off for the purpose of testing the background systematics that may also affect the axion search.

CADEx will provide a multidisciplinary platform to develop novel concepts of haloscopes, including tunable-cavity haloscopes, and push the W-band superconducting detectors to their ultimate sensitivities, which are crucial to confirm or rule out the QCD axion predicted by the models with a mass in the range 330–460 µeV.

Acknowledgments

We thank RADES team members for inspiring discussions. SA and JM are supported by grants PID2019-108122GB-C32 and the Maria de Maeztu grant CEX-2019-000918-M of ICCUB. The work of UPCT and IFIC is supported by grant PID2019-108122GB-C33, funded by MCIN/AEI/10.13039/501100011033/ and by "ERDF A way of making Europe". JMGB thanks the grant FPI BES-2017-079787, funded by MCIN/AEI/10.13039/501100011033 and by "ESF Investing in your future". The work of Universidad de Cantabria is supported by the Ministry of Science and Innovation under Grant PID2019-110610RB-C22. CAB and IMDEA-Nanoscience work is supported by grants PID2019-105552RB-C41 and PID2019-105552RB-C44 and by Comunidad de Madrid under Grant P2018/NMT-4291. IMDEA-Nanoscience acknowledges financial support from "Severo Ochoa" Programme for Centers of Excellence in R&D (MINECO, Grant SEV-2016-0686). D.G. and A.G also acknowledge Grant DEFROST N62909-19-1-2053 from ONR Global. RBB, FJC, BJK, EMG, JMS and PV thank the Spanish Agencia Estatal de Investigación (AEI, MICIU) for the support to the Unidad de Excelencia María de Maeztu Instituto de Física de Cantabria, ref. MDM-2017-0765. RBB, FJC, EMG and PV thank the Spanish Agencia Estatal de Investigación (AEI, MCI) for the funds received through the research project, ref. PID2019-110610RB-C21. RBB, FJC, BJK, EMG, JMS and PV also thank the 'Dark Collaboration at IFCA' working group for useful discussions. The work done by ANTERAL S.L. is supported by project QON-Space financed by the Navarra Government Project No. 0011-1365-2021-000220. UPNA acknowledges financial support from the Spanish State Research Agency, Project No. PID2019-109984RB-C43/AEI/10.13039/501100011033 and Project No. PID2020-112545RB-C53/MCIN/AEI/ 10.13039/501100011033.

References

[1] G. Bertone, D. Hooper and J. Silk, *Particle dark matter: evidence, candidates and constraints*, *Phys. Rept.* **405** (2005) 279 [hep-ph/0404175] [INSPIRE].

[2] D. Clowe et al., *A direct empirical proof of the existence of dark matter*, *Astrophys. J. Lett.* **648** (2006) L109 [astro-ph/0608407] [INSPIRE].

[3] PLANCK collaboration, *Planck* 2018 *results. VI. Cosmological parameters*, *Astron. Astrophys.* **641** (2020) A6 [*Erratum ibid.* **652** (2021) C4] [arXiv:1807.06209] [INSPIRE].

[4] R.D. Peccei, *The strong CP problem and axions*, *Lect. Notes Phys.* **741** (2008) 3 [hep-ph/0607268] [INSPIRE].

[5] J. Billard et al., *Direct detection of dark matter — APPEC committee report*, *Rept. Prog. Phys.* **85** (2022) 056201 [arXiv:2104.07634] [INSPIRE].

[6] C.G. Callan, Jr., R.F. Dashen and D.J. Gross, *The structure of the gauge theory vacuum*, *Phys. Lett. B* **63** (1976) 334 [INSPIRE].

[7] C. Abel et al., *Measurement of the permanent electric dipole moment of the neutron*, *Phys. Rev. Lett.* **124** (2020) 081803 [arXiv:2001.11966] [INSPIRE].

[8] R.D. Peccei and H.R. Quinn, *CP conservation in the presence of instantons*, *Phys. Rev. Lett.* **38** (1977) 1440 [INSPIRE].

[9] R.D. Peccei and H.R. Quinn, *Constraints imposed by CP conservation in the presence of instantons*, *Phys. Rev. D* **16** (1977) 1791 [INSPIRE].

[10] F. Wilczek, *Problem of strong P and T invariance in the presence of instantons*, *Phys. Rev. Lett.* **40** (1978) 279 [INSPIRE].

[11] S. Weinberg, *A new light boson?*, *Phys. Rev. Lett.* **40** (1978) 223 [INSPIRE].

[12] L. Visinelli and P. Gondolo, *Dark matter axions revisited*, *Phys. Rev. D* **80** (2009) 035024 [arXiv:0903.4377] [INSPIRE].

[13] L. Visinelli and P. Gondolo, *Axion cold dark matter in non-standard cosmologies*, *Phys. Rev. D* **81** (2010) 063508 [arXiv:0912.0015] [INSPIRE].

[14] J.E. Kim, *Weak interaction singlet and strong CP invariance*, *Phys. Rev. Lett.* **43** (1979) 103 [INSPIRE].

[15] M.A. Shifman, A.I. Vainshtein and V.I. Zakharov, *Can confinement ensure natural CP invariance of strong interactions?*, *Nucl. Phys. B* **166** (1980) 493 [INSPIRE].

[16] M. Dine, W. Fischler and M. Srednicki, *A simple solution to the strong CP problem with a harmless axion*, *Phys. Lett. B* **104** (1981) 199 [INSPIRE].

[17] A.R. Zhitnitsky, *On possible suppression of the axion hadron interactions*, *Sov. J. Nucl. Phys.* **31** (1980) 260 [*Yad. Fiz.* **31** (1980) 497] [INSPIRE].

[18] J. Preskill, M.B. Wise and F. Wilczek, *Cosmology of the invisible axion*, *Phys. Lett. B* **120** (1983) 127 [INSPIRE].

[19] L.F. Abbott and P. Sikivie, *A cosmological bound on the invisible axion*, *Phys. Lett. B* **120** (1983) 133 [INSPIRE].

[20] M. Dine and W. Fischler, *The not so harmless axion*, *Phys. Lett. B* **120** (1983) 137 [INSPIRE].

[21] D.J.E. Marsh, *Axion cosmology*, *Phys. Rept.* **643** (2016) 1 [arXiv:1510.07633] [INSPIRE].

[22] C. Bonati et al., *Axion phenomenology and θ-dependence from $N_f = 2 + 1$ lattice QCD*, *JHEP* **03** (2016) 155 [arXiv:1512.06746] [INSPIRE].

[23] P. Petreczky, H.-P. Schadler and S. Sharma, *The topological susceptibility in finite temperature QCD and axion cosmology*, *Phys. Lett. B* **762** (2016) 498 [arXiv:1606.03145] [INSPIRE].

[24] E. Berkowitz, M.I. Buchoff and E. Rinaldi, *Lattice QCD input for axion cosmology*, *Phys. Rev. D* **92** (2015) 034507 [arXiv:1505.07455] [INSPIRE].

[25] L. Fleury and G.D. Moore, *Axion dark matter: strings and their cores*, *JCAP* **01** (2016) 004 [arXiv:1509.00026] [INSPIRE].

[26] G. Ballesteros, J. Redondo, A. Ringwald and C. Tamarit, *Unifying inflation with the axion, dark matter, baryogenesis and the seesaw mechanism*, *Phys. Rev. Lett.* **118** (2017) 071802 [arXiv:1608.05414] [INSPIRE].

[27] S. Borsányi et al., *Calculation of the axion mass based on high-temperature lattice quantum chromodynamics*, *Nature* **539** (2016) 69 [arXiv:1606.07494] [INSPIRE].

[28] M. Dine, P. Draper, L. Stephenson-Haskins and D. Xu, *Axions, instantons, and the lattice*, *Phys. Rev. D* **96** (2017) 095001 [arXiv:1705.00676] [INSPIRE].

[29] V.B.. Klaer and G.D. Moore, *The dark-matter axion mass*, *JCAP* **11** (2017) 049 [arXiv:1708.07521] [INSPIRE].

[30] M. Buschmann, J.W. Foster and B.R. Safdi, *Early-universe simulations of the cosmological axion*, *Phys. Rev. Lett.* **124** (2020) 161103 [arXiv:1906.00967] [INSPIRE].

[31] M. Buschmann et al., *Dark matter from axion strings with adaptive mesh refinement*, *Nature Commun.* **13** (2022) 1049 [arXiv:2108.05368] [INSPIRE].

[32] H. Primakoff, *Photoproduction of neutral mesons in nuclear electric fields and the mean life of the neutral meson*, *Phys. Rev.* **81** (1951) 899 [INSPIRE].

[33] P. Sikivie, *Experimental tests of the invisible axion*, *Phys. Rev. Lett.* **51** (1983) 1415 [*Erratum ibid.* **52** (1984) 695] [INSPIRE].

[34] CAST collaboration, *First results of the CAST-RADES haloscope search for axions at 34.67 μeV*, *JHEP* **21** (2020) 075 [arXiv:2104.13798] [INSPIRE].

[35] J. Jeong, S. Youn, S. Ahn, J.E. Kim and Y.K. Semertzidis, *Concept of multiple-cell cavity for axion dark matter search*, *Phys. Lett. B* **777** (2018) 412 [arXiv:1710.06969] [INSPIRE].

[36] J. Choi, S. Ahn, B.R. Ko, S. Lee and Y.K. Semertzidis, *CAPP-8TB: axion dark matter search experiment around* 6.7 μeV, *Nucl. Instrum. Meth. A* **1013** (2021) 165667 [arXiv:2007.07468] [INSPIRE].

[37] ADMX collaboration, *A search for invisible axion dark matter with the Axion Dark Matter Experiment*, *Phys. Rev. Lett.* **120** (2018) 151301 [arXiv:1804.05750] [INSPIRE].

[38] ADMX collaboration, *Extended search for the invisible axion with the Axion Dark Matter Experiment*, *Phys. Rev. Lett.* **124** (2020) 101303 [arXiv:1910.08638] [INSPIRE].

[39] ADMX collaboration, *Piezoelectrically tuned multimode cavity search for axion dark matter*, *Phys. Rev. Lett.* **121** (2018) 261302 [arXiv:1901.00920] [INSPIRE].

[40] HAYSTAC collaboration, *Results from phase* 1 *of the HAYSTAC microwave cavity axion experiment*, *Phys. Rev. D* **97** (2018) 092001 [arXiv:1803.03690] [INSPIRE].

[41] HAYSTAC collaboration, *A quantum-enhanced search for dark matter axions*, *Nature* **590** (2021) 238 [arXiv:2008.01853] [INSPIRE].

[42] D. Alesini et al., *Galactic axions search with a superconducting resonant cavity*, *Phys. Rev. D* **99** (2019) 101101 [arXiv:1903.06547] [INSPIRE].

[43] D. Alesini et al., *Search for invisible axion dark matter of mass* $m_a = 43\,\mu eV$ *with the QUAX-*$a\gamma$ *experiment*, *Phys. Rev. D* **103** (2021) 102004 [arXiv:2012.09498] [INSPIRE].

[44] B.T. McAllister et al., *The ORGAN experiment: an axion haloscope above* 15 *GHz*, *Phys. Dark Univ.* **18** (2017) 67 [arXiv:1706.00209] [INSPIRE].

[45] T. Grenet et al., *The Grenoble Axion Haloscope platform (GrAHal): development plan and first results*, arXiv:2110.14406 [INSPIRE].

[46] M. Lawson, A.J. Millar, M. Pancaldi, E. Vitagliano and F. Wilczek, *Tunable axion plasma haloscopes*, *Phys. Rev. Lett.* **123** (2019) 141802 [arXiv:1904.11872] [INSPIRE].

[47] A.J. Millar, G.G. Raffelt, J. Redondo and F.D. Steffen, *Dielectric haloscopes to search for axion dark matter: theoretical foundations*, *JCAP* **01** (2017) 061 [arXiv:1612.07057] [INSPIRE].

[48] S. Beurthey et al., *MADMAX status report*, arXiv:2003.10894 [INSPIRE].

[49] D. Horns, J. Jaeckel, A. Lindner, A. Lobanov, J. Redondo and A. Ringwald, *Searching for WISPy cold dark matter with a dish antenna*, *JCAP* **04** (2013) 016 [arXiv:1212.2970] [INSPIRE].

[50] BREAD collaboration, *Broadband solenoidal haloscope for terahertz axion detection*, *Phys. Rev. Lett.* **128** (2022) 131801 [arXiv:2111.12103] [INSPIRE].

[51] I.G. Irastorza and J. Redondo, *New experimental approaches in the search for axion-like particles*, *Prog. Part. Nucl. Phys.* **102** (2018) 89 [arXiv:1801.08127] [INSPIRE].

[52] Y.K. Semertzidis and S. Youn, *Axion dark matter: how to see it?*, *Sci. Adv.* **8** (2022) abm9928 [arXiv:2104.14831] [INSPIRE].

[53] P. Sikivie, *Invisible axion search methods*, *Rev. Mod. Phys.* **93** (2021) 015004 [arXiv:2003.02206] [INSPIRE].

[54] M. Fabbrichesi, E. Gabrielli and G. Lanfranchi, *The dark photon*, arXiv:2005.01515 [INSPIRE].

[55] S. Ghosh, E.P. Ruddy, M.J. Jewell, A.F. Leder and R.H. Maruyama, *Searching for dark photons with existing haloscope data*, *Phys. Rev. D* **104** (2021) 092016 [arXiv:2104.09334] [INSPIRE].

[56] A. Caputo, A.J. Millar, C.A.J. O'Hare and E. Vitagliano, *Dark photon limits: a handbook*, *Phys. Rev. D* **104** (2021) 095029 [arXiv:2105.04565] [INSPIRE].

[57] A.E. Nelson and J. Scholtz, *Dark light, dark matter and the misalignment mechanism*, *Phys. Rev. D* **84** (2011) 103501 [arXiv:1105.2812] [INSPIRE].

[58] P. Arias, D. Cadamuro, M. Goodsell, J. Jaeckel, J. Redondo and A. Ringwald, *WISPy cold dark matter*, *JCAP* **06** (2012) 013 [arXiv:1201.5902] [INSPIRE].

[59] G. Alonso-Álvarez, T. Hugle and J. Jaeckel, *Misalignment & co.: (pseudo-)scalar and vector dark matter with curvature couplings*, *JCAP* **02** (2020) 014 [arXiv:1905.09836] [INSPIRE].

[60] *Laboratorio Subterráneo Canfranc — LSC webpage*, https://lsc-canfranc.es/en, July 2020.

[61] C.M. Caves, *Quantum limits on noise in linear amplifiers*, *Phys. Rev. D* **26** (1982) 1817 [INSPIRE].

[62] F. Tercero et al., *Yebes 40 m radio telescope and the broad band nanocosmos receivers at 7 mm and 3 mm for line surveys*, *Astron. Astrophys.* **645** (2021) A37.

[63] P. Yagoubov et al., *Wideband 67–116 GHz receiver development for ALMA band 2*, *Astron. Astrophys.* **634** (2020) A46 [arXiv:1912.10841] [INSPIRE].

[64] M.W. Pospieszalski, *Extremely low-noise cryogenic amplifiers for radio astronomy: past, present and future*, in 2018 22$^{\text{nd}}$ *international microwave and radar conference (MIKON)*, IEEE, (2018).

[65] S. Leclercq, *Discussion about noise equivalent power and its use for photon noise calculation*, in *report on FOV optics and bolometer projects for the 30 m telescope*, International Research Institute For Radio Astronomy (IRAM) (2007), p. 1.

[66] G. Ulbricht, M.D. Lucia and E. Baldwin, *Applications for microwave kinetic induction detectors in advanced instrumentation*, *Appl. Sci.* **11** (2021) 2671.

[67] P.C. Nagler, J.E. Sadleir and E.J. Wollack, *Transition-edge sensor detectors for the origins space telescope*, *J. Astron. Telescopes Instrum. Syst.* **7** (2021) 011005.

[68] B.S. Karasik and R. Cantor, *Optical NEP in hot-electron nanobolometers*, *Appl. Phys. Lett.* **98** (2011) 193503 [arXiv:1009.4676] [INSPIRE].

[69] P.J. de Visser, J.J.A. Baselmans, J. Bueno, N. Llombart and T.M. Klapwijk, *Fluctuations in the electron system of a superconductor exposed to a photon flux*, *Nature Commun.* **5** (2014) 1.

[70] A. Endo et al., *Wideband on-chip terahertz spectrometer based on a superconducting filterbank*, *J. Astron. Telescopes Instrum. Syst.* **5** (2019) 035004.

[71] ADMX collaboration, *Results from a high sensitivity search for cosmic axions*, *Phys. Rev. Lett.* **80** (1998) 2043 [astro-ph/9801286] [INSPIRE].

[72] S. Hailey-Dunsheath et al., *Kinetic inductance detectors for the origins space telescope*, *J. Astron. Telescopes Instrum. Syst.* **7** (2021) 011015.

[73] R. Adam et al., *The NIKA2 large-field-of-view millimetre continuum camera for the 30 m IRAM telescope*, *Astron. Astrophys.* **609** (2018) A115 [arXiv:1707.00908] [INSPIRE].

[74] S. Masi et al., *Kinetic inductance detectors for the OLIMPO experiment: in-flight operation and performance*, *JCAP* **07** (2019) 003 [arXiv:1902.08993] [INSPIRE].

[75] K. Karatsu et al., *Mitigation of cosmic ray effect on microwave kinetic inductance detector arrays*, *Appl. Phys. Lett.* **114** (2019) 032601 [arXiv:1901.02387] [INSPIRE].

[76] Particle Data Group collaboration, *Review of particle physics*, *PTEP* **2022** (2022) 083C01 [INSPIRE].

[77] P. Sikivie, *Experimental tests of the invisible axion*, *Phys. Rev. Lett.* **51** (1983) 1415 [*Erratum ibid.* **52** (1984) 695] [INSPIRE].

[78] L. Krauss, J. Moody, F. Wilczek and D.E. Morris, *Calculations for cosmic axion detection*, *Phys. Rev. Lett.* **55** (1985) 1797 [INSPIRE].

[79] S. Al Kenany et al., *Design and operational experience of a microwave cavity axion detector for the* 20–100 μeV *range*, *Nucl. Instrum. Meth. A* **854** (2017) 11 [arXiv:1611.07123] [INSPIRE].

[80] A. Díaz-Morcillo et al., *Design of new resonant haloscopes in the search for the dark matter axion: a review of the first steps in the RADES collaboration*, *Universe* **8** (2021) 5 [arXiv:2111.14510] [INSPIRE].

[81] C.A. Balanis, *Advanced engineering electromagnetics*, John Wiley & Sons (1989).

[82] R.E. Collin, *Foundations for microwave engineering*, second edition, IEEE Press (2001).

[83] D. Kim, J. Jeong, S. Youn, Y. Kim and Y.K. Semertzidis, *Revisiting the detection rate for axion haloscopes*, *JCAP* **03** (2020) 066 [arXiv:2001.05605] [INSPIRE].

[84] W. Larson and R.D. Hunter, *A broadband noncontacting sliding short*, NBS technical note 602, (1971).

[85] ADMX collaboration, *Axion Dark Matter Experiment: detailed design and operations*, *Rev. Sci. Instrum.* **92** (2021) 124502 [arXiv:2010.00169] [INSPIRE].

[86] P.K. Day, H.G. LeDuc, B.A. Mazin, A. Vayonakis and J. Zmuidzinas, *A broadband superconducting detector suitable for use in large arrays*, *Nature* **425** (2003) 817.

[87] A. Catalano et al., *Sensitivity of LEKID for space applications between* 80 *GHz and* 600 *GHz*, *Astron. Astrophys.* **641** (2020) A179 [arXiv:2006.14991] [INSPIRE].

[88] M. Calvo et al., *The NIKA2 instrument, a dual-band kilopixel KID array for millimetric astronomy*, *J. Low Temp. Phys.* **184** (2016) 816 [arXiv:1601.02774] [INSPIRE].

[89] J. van Rantwijk, M. Grim, D. van Loon, S. Yates, A. Baryshev and J. Baselmans, *Multiplexed readout for* 1000*-pixel arrays of microwave kinetic inductance detectors*, *IEEE Trans. Microwave Theory Tech.* **64** (2016) 1876.

[90] E. O'Connor, A. Shearer and K. O'Brien, *Energy-sensitive detectors for astronomy: past, present and future*, *New Astron. Rev.* **87** (2019) 101526.

[91] L. Cardani et al., *Final results of CALDER: kinetic inductance light detectors to search for rare events*, *Eur. Phys. J. C* **81** (2021) 636 [arXiv:2104.06850] [INSPIRE].

[92] I. Colantoni et al., *BULLKID: BULky and Low-threshold Kinetic Inductance Detectors*, *J. Low Temp. Phys.* **199** (2020) 593 [INSPIRE].

[93] B. Aja et al., *Analysis and performance of lumped-element kinetic inductance detectors for w-band*, *IEEE Trans. Microwave Theory Tech.* **69** (2021) 578.

[94] S. Shu, M. Calvo, S. Leclercq, J. Goupy, A. Monfardini and E.F.C. Driessen, *Prototype high angular resolution LEKIDs for NIKA2*, *J. Low Temp. Phys.* **193** (2018) 141.

[95] D. Flanigan et al., *Magnetic field dependence of the internal quality factor and noise performance of lumped-element kinetic inductance detectors*, *Appl. Phys. Lett.* **109** (2016) 143503 [arXiv:1609.06352] [INSPIRE].

[96] A.A. Melcón et al., *Axion searches with microwave filters: the RADES project*, *JCAP* **05** (2018) 040 [arXiv:1803.01243] [INSPIRE].

[97] A. Álvarez Melcón et al., *Scalable haloscopes for axion dark matter detection in the* 30 μeV *range with RADES*, *JHEP* **07** (2020) 084 [arXiv:2002.07639] [INSPIRE].

[98] CAST collaboration, *New CAST limit on the axion-photon interaction*, *Nature Phys.* **13** (2017) 584 [arXiv:1705.02290] [INSPIRE].

[99] S. De Panfilis et al., *Limits on the abundance and coupling of cosmic axions at* $4.5 < m_a < 5.0\,\mu eV$, *Phys. Rev. Lett.* **59** (1987) 839 [INSPIRE].

[100] C. Hagmann, P. Sikivie, N.S. Sullivan and D.B. Tanner, *Results from a search for cosmic axions*, *Phys. Rev. D* **42** (1990) 1297 [INSPIRE].

[101] ADMX collaboration, *Piezoelectrically tuned multimode cavity search for axion dark matter*, *Phys. Rev. Lett.* **121** (2018) 261302 [arXiv:1901.00920] [INSPIRE].

[102] HAYSTAC collaboration, *Results from phase 1 of the HAYSTAC microwave cavity axion experiment*, *Phys. Rev. D* **97** (2018) 092001 [arXiv:1803.03690] [INSPIRE].

[103] CAPP collaboration, *First results from an axion haloscope at CAPP around* $10.7\,\mu eV$, *Phys. Rev. Lett.* **126** (2021) 191802 [arXiv:2012.10764] [INSPIRE].

[104] ADMX collaboration, *Search for invisible axion dark matter in the* 3.3–$4.2\,\mu eV$ *mass range*, *Phys. Rev. Lett.* **127** (2021) 261803 [arXiv:2110.06096] [INSPIRE].

[105] J.W. Foster et al., *Extraterrestrial axion search with the breakthrough listen galactic center survey*, arXiv:2202.08274 [INSPIRE].

[106] C. O'Hare, *cajohare/axionlimits: axionlimits*, Zenodo (2020).

[107] D. Ahn et al., *Biaxially textured* $\mathrm{yba_2cu_3o_{7-x}}$ *microwave cavity in a high magnetic field for a dark-matter axion search*, *Phys. Rev. Applied* **17** (2022) L061005.

[108] L. Di Luzio, F. Mescia and E. Nardi, *Redefining the axion window*, *Phys. Rev. Lett.* **118** (2017) 031801 [arXiv:1610.07593] [INSPIRE].

[109] L. Di Luzio, F. Mescia and E. Nardi, *Window for preferred axion models*, *Phys. Rev. D* **96** (2017) 075003 [arXiv:1705.05370] [INSPIRE].

[110] P. Agrawal, J. Fan, M. Reece and L.-T. Wang, *Experimental targets for photon couplings of the QCD axion*, *JHEP* **02** (2018) 006 [arXiv:1709.06085] [INSPIRE].

[111] I. Stern, *ADMX status*, *PoS* **ICHEP2016** (2016) 198 [arXiv:1612.08296] [INSPIRE].

[112] R.T. Co, A. Pierce, Z. Zhang and Y. Zhao, *Dark photon dark matter produced by axion oscillations*, *Phys. Rev. D* **99** (2019) 075002 [arXiv:1810.07196] [INSPIRE].

[113] M. Bastero-Gil, J. Santiago, L. Ubaldi and R. Vega-Morales, *Vector dark matter production at the end of inflation*, *JCAP* **04** (2019) 015 [arXiv:1810.07208] [INSPIRE].

[114] P. Agrawal, N. Kitajima, M. Reece, T. Sekiguchi and F. Takahashi, *Relic abundance of dark photon dark matter*, *Phys. Lett. B* **801** (2020) 135136 [arXiv:1810.07188] [INSPIRE].

[115] R.T. Co, K. Harigaya and A. Pierce, *Gravitational waves and dark photon dark matter from axion rotations*, *JHEP* **12** (2021) 099 [arXiv:2104.02077] [INSPIRE].

[116] P. Brun, L. Chevalier and C. Flouzat, *Direct searches for hidden-photon dark matter with the SHUKET experiment*, *Phys. Rev. Lett.* **122** (2019) 201801 [arXiv:1905.05579] [INSPIRE].

[117] L.H. Nguyen, A. Lobanov and D. Horns, *First results from the WISPDMX radio frequency cavity searches for hidden photon dark matter*, *JCAP* **10** (2019) 014 [arXiv:1907.12449] [INSPIRE].

[118] N. Tomita et al., *Search for hidden-photon cold dark matter using a K-band cryogenic receiver*, *JCAP* **09** (2020) 012 [arXiv:2006.02828] [INSPIRE].

[119] A.V. Dixit et al., *Searching for dark matter with a superconducting qubit*, *Phys. Rev. Lett.* **126** (2021) 141302 [arXiv:2008.12231] [INSPIRE].

[120] B. Godfrey et al., *Search for dark photon dark matter: dark E field radio pilot experiment*, *Phys. Rev. D* **104** (2021) 012013 [arXiv:2101.02805] [INSPIRE].